Iodine Uptake by Zr/Hf-Based UiO-66 Materials: The Influence of Metal Substitution on Iodine Evolution

Pedro H M Andrade, Natacha Henry, Christophe Volkringer, Thierry Loiseau, Hervé Vezin, Matthieu Hureau, Alain Moissette

Iodine Uptake by Zr/Hf-Based UiO-66 Materials: The Influence of Metal Substitution on Iodine Evolution

Pedro H. M. Andrade[1,•,*], Natacha Henry[2], Christophe Volkringer[2,□], Thierry Loiseau[2,⊥], Hervé Vezin[1,°], Matthieu Hureau[1], Alain Moissette[1,⋆,*]

(1) Laboratoire de Spectroscopie pour les Interactions, la Réactivité et l'Environnement (LASIRE), Université de Lille – Sciences et Technologies, 59655 - Villeneuve d'Ascq, France.

(2) Unité de Catalyse et Chimie du Solide (UCCS), Univ. Lille, CNRS, Centrale Lille, Univ. Artois, UMR 8181, F-59000 Lille, France

* corresponding authors

• pedro.moraisandrade@univ-lille.fr – ORCID: **0000-0002-8264-1818**

□ christophe.volkringer@centralelille.fr – ORCID: **0000-0003-2769-9360**

⊥ thierry.loiseau@univ-lille.fr – ORCID: **0000-0001-8175-3407**

° herve.vezin@univ-lille.fr– ORCID: **0000-0001-8175-3407**

⋆ alain.moissette@univ-lille.fr – ORCID: **0000-0003-2713-5143**

ABSTRACT

KEYWORDS: UiO-66; MOF; Iodine; Spectroscopy; Zirconium; Hafnium.

Many works reported the encapsulation of iodine in Metal-Organic Frameworks (MOFs) as well as the $I_2 \rightarrow I_3^-$ chemical conversion. This transformation has been examined by adsorbing gaseous iodine on a series of UiO-66 materials and the different Hf/Zr metal ratios (0-100% Hf) were evaluated during the evolution of I_2 into I_3^-. The influence of the hafnium content on the UiO-66 structure was highlighted by PXRD, SEM images, and gas sorption tests. The UiO-66(Hf) presented smaller lattice parameter (a = 20.7232(7) Å), higher crystallite size ($0.18 \leq \Phi \leq 3.33$ µm), and smaller SSA_{BET} (818(24) $m^2.g^{-1}$) when compared to its parent UiO-66(Zr) – a = 20.7696(8) Å, $100 \leq \Phi \leq 250$ nm, and SSA_{BET} = (1262(33) $m^2.g^{-1}$). The effect of replacing Zr atoms by Hf in the physical properties of the UiO-66 was deeply evaluated by a spectroscopic study using UV-vis, FTIR, and Raman characterizations. In this case, the Hf presence reduced the band gap of the UiO-66, from 4.07 eV in UiO-66(Zr) to 3.98 eV in UiO-66(Hf). Furthermore, the UiO-66(Hf) showed a blue-shift for several FTIR and Raman bands, indicating a stiffening on the implied interatomic bonds when comparing to UiO-66(Zr) spectra. Hafnium was found to clearly favorize the capture of iodine (285 $g.mol^{-1}$, against 230 $g.mol^{-1}$ for UiO-66(Zr)) and the kinetic evolution of I_2 into I_3^- after 16 hours of I_2 filtration. Three iodine species were typically identified by Raman spectroscopy and chemometric analysis. These species are: "free" I_2 (206 cm^{-1}), "perturbed" I_2 (173 cm^{-1}) and I_3^- (115 and 141 cm^{-1}). It was also verified, by FTIR spectroscopy, that the oxo and hydroxyl groups of the inorganic $[M_6O_4(OH)_4]$ (M = Zr, Hf) cluster were perturbed after the adsorption of I_2 into UiO-66(Hf), which was ascribed to the higher acid character of Hf. Finally, with that in mind and considering that the EPR results discard the possibility of a redox phenomenon involving the tetravalent cations (Hf^{4+} or Zr^{4+}), a mechanism was proposed for the conversion of I_2 into I_3^- in UiO-66 – based on an electron donor-acceptor complex between the aromatic ring of the BDC linker and the I_2 molecule.

1. INTRODUCTION

The use of radioactive compounds for medical purposes has been widely employed, worth mentioning the use of ^{123}I for diagnostic and therapeutic purposes [1,2]. However, other iodine radioisotopes such as ^{129}I and ^{131}I can be released into the geosphere environment during nuclear accidents and in the course of the reprocessing of Used Nuclear Fuel (UNF), causing great damage to fauna and to flora [3]. ^{129}I raises concern during UNF reprocessing due to its long half-life time ($t_{1/2} = 1.6 \times 10^7$ years) and high mobility in most geological environments [3]. On the other hand, ^{131}I raises concerns in nuclear accidents because of its high specific activity (4.59×10^{15} $Bq.g^{-1}$) and potential to be captured by the thyroid, being incorporated into human metabolic processes [3,4]. It is worth mentioning that those species are normally released in its gaseous form (I_2) and also as organic-iodine compounds (CH_3I) [5].

Some materials can be used to trap the gaseous I_2, notably Metal-Organic Frameworks (MOFs), which is a class of hybrid materials formed by inorganic polyoxo clusters that are connected to each other by organic linkers, forming organized and open crystalline networks [6,7]. They are known for their high specific surface areas (SSA), permanent nanocrystalline porous structure and for the possibility of being chemically modified – by functionalizing their pores, by changing their metal clusters and/or by replacing their organic linkers [8,9]. There are procedures reported in the literature that can be used to modify these materials through post-synthetic modifications (PSM), which allows the development of many different kinds of MOFs that cannot be obtained by direct solvothermal routes [10].

Zirconium-based MOFs are widely studied due to their high stability in severe chemical environments, such as acid and basic media [11]. One can cite the topology UiO-66, which is synthesized from the mixture of $ZrCl_4$ and 1,4-benzenedicarboxylic acid (H_2BDC, also known as terephthalic acid) in *N*,*N*-dimethylformamide solvent [12]. It presents a three-dimensional

framework defining a face centered cubic unit that consists of inorganic $Zr_6O_4(OH)_4$ bricks, 12-fold connected to the lattice through the BDC linkers to the Zr-nodes [13]. A parent structure from UiO-66(Zr) is also reported in the literature and can be obtained by changing the metal precursor to $HfCl_4$ [14]. Finally, bimetallic UiO-66 materials were also reported elsewhere with composition variation $\{Zr_xHf_{6-x}\}$ for the inorganic core [15]. UiO-66(Hf) exhibits similar physical-chemical properties to those of UiO-66(Zr) since both metals – zirconium and hafnium – are part of the same group elements (column IV of the periodic table) with the same tetravalent oxidation state. However, it is expected that Hf-based MOFs offer higher acidic behavior than their isostructural Zr-based MOFs, since the dissociation enthalpies of Hf–O bonds are higher than those of Zr–O (802 vs. 776 $kJ.mol^{-1}$) [16–18].

UiO-66 family was employed in this work to retain radioactive I_2, as a recent study demonstrated the iodine-131 adsorption capacity of an amino-functionalized UiO-66 MOF [19]. It also highlighted its stability under conditions that simulates ^{131}I leaking during nuclear accidents (steam at 120 ºC and γ radiation from ^{60}Co source up to 2 MGy) [19]. Moreover, due to the facility of being chemically modified, the UiO-66 family reveals to be a great candidate for evaluating the effects of functionalizing their organic linkers and/or of replacing their metallic sites on its capacity to retain iodine. For instance, aiming to understand the linker influence over the I_2 capture, some isoreticular structures of UiO-66, UiO-67, and UiO-68 were explored in another work [20], which mentioned a transformation from I_2 into I_3^- that took place after the contact between the gaseous iodine and the UiO materials. The effect of the presence of amino groups attached to the aromatic ring of the linker, has been reported, and indicated the enhancement of the of $I_2 \rightarrow I_3^-$ conversion rate. This reaction was monitored by using UV-vis and Raman spectroscopy; however, its mechanism was not explicated in detail. Furthermore, to this day and to the best of the authors' knowledge, there is no mention in the literature of a deep spectroscopy study that relates the influence of the metal nature in the UiO-66 structure with the capture of iodine. Thus, since the iodine uptake and the charge-transfer complexes inside the UiO-66 are expected to be influenced

by the metal cluster (as the band gap of UiO-66 depends on this parameter) [21], this effect is to be evaluated. In this work, hafnium was chosen for replacing zirconium in UiO-66 due to its higher acidity and similar characteristics, as they are part of the same family in the periodic table. Additionally, the $I_2 \rightarrow I_3^-$ conversion mechanism involving a redox reaction inside this MOF is not yet elucidated. This emphasizes the importance of a deeply understanding over the metal influence on the physical-chemical properties of the UiO-66 series incorporating zirconium and/or hafnium. This study employs several characterization techniques such as scanning electron microscopy (SEM), energy-dispersive X-ray spectroscopy (EDS), Fourier transform infrared spectroscopy (FTIR), Raman spectroscopy, diffuse reflectance UV-Vis spectroscopy, powder X-ray diffraction (PXRD), electron paramagnetic resonance (EPR), and N_2 sorption to characterize the UiO-66(Zr:Hf) obtained materials.

2. MATERIALS AND METHODS

2.1 SYNTHESES AND ACTIVATION

UiO-66(Zr) was prepared by solvothermal treatment as follows: zirconium chloride ($ZrCl_4$, Sigma Aldrich 99.9%, 2.0 g, 8.58 mmol), terephthalic acid ($(COOH)_2C_6H_4$, Sigma Aldrich, 98%, 2.8 g, 16.85 mmol), formic acid (HCOOH, 32.5 mL) and *N*,*N*-dimethylformamide (DMF, 163 mL) were initially added in a 250 mL glass bottle, which was then placed in an oven. After raising temperature for 1h, the system was kept at 120 ºC for 24 h. A white solid was recovered by centrifugation after natural cooling of the bottle. Then, it was washed three times with fresh DMF and three times with fresh ethanol. Finally, it was calcined in air at 100 ºC for 1 h and then 150 ºC for 18 h for the activation step. After the last stage, 2.5 g of UiO-66(Zr) was collected and kept in a flask under Ar atmosphere in a glovebox (JACOMEX, GP Campus series).

UiO-66(Hf) was solvothermally prepared as well. Hafnium chloride ($HfCl_4$, Sigma Aldrich 99.9%, 2.75 g, 8.58 mmol), terephthalic acid ($(COOH)_2C_6H_4$, Sigma Aldrich, 98%, 2.8 g, 16.85 mmol), formic acid (HCOOH, 32.5 mL) and dimethylformamide (DMF, 163 mL) were initially added in a 250 mL glass bottle and the following procedure is identical to that described above for UiO-66(Zr). After the last stage, 2.5 g of UiO-66(Hf) was collected and kept in a flask under Ar atmosphere.

The other three samples of UiO-66(Hf/Zr) series followed the same synthesis procedure while respecting the molar desired Hf/Zr ratio. Shortly, the $HfCl_4$ and $ZrCl_4$ salts were pre-mixed in molar proportions of 1:3, 1:1, and 3:1, based on a total 8.58 mmol for $HfCl_4$ + $ZrCl_4$. The molar ratio between the total amount of metal precursors and the other reactants was maintained in all syntheses. The other stages followed as previously described. The mass of solid collected after drying was about 2.5 g for each Hf/Zr composition and was kept in glass flasks under Ar atmosphere. It is worth mentioning that the percentages of Hf and Zr presented in this work are always related only to the metal atoms (i.e., the UiO-66(25% Hf) presents 19% Hf and 81% Zr over a total of 100% metal atoms). Also, the UiO-66 structure is exhibited in Figure S1, as well as their main cavities.

2.2 STRUCTURAL CHARACTERIZATION

Inductively coupled plasma - optical emission spectrometry: Inductively coupled plasma - optical emission spectrometry (ICP-OES) experiments were conducted using an Agilent 5110 ICP-OES spectrometer in radial sighting mode. The mineralization of the samples was performed using 100 mg of the activated UiO-66 compounds. First, the powdered samples were digested using a solution containing 10 mL of HF and 5 mL of HNO_3 and then they were heated to 140 ºC for 48 h, followed by a dry evaporation step. Next, they were etched with aqua regia (HNO_3:HCl 3:6 mL), heated to 120 ºC for 24 h and dried to a residue of 0.5 mL Finally, 9.5 mL of water was

added and, after filtration, the solution was diluted at 1/100 before being analyzed using the 264.141 nm and 343.823 nm emission lines of hafnium and zirconium, respectively.

X-ray diffraction: Powder X-ray Diffraction (PXRD) experiments were done using a SmartLab Rigaku diffractometer equipped with a 9 kW rotating anode X-ray generator (Cu $K\alpha_1$ = 1.5418 Å), endowed with a HyPix-3000 hybrid multi-dimensional pixel detector, using capillaries in parallel transmission geometry. The 2θ scans were performed in the range 5°-70°, with a step size of 0.01° and a speed of 3°/min.

Surface area measurement: N_2 sorption was performed at liquid nitrogen temperature (77K) using a Micromeritics ASAP2020 apparatus using samples previously degassed under vacuum at 150 °C. The specific surface area and pore size distribution of the examined samples were evaluated by the multipoint BET (Brunauer–Emmett–Teller) model in the 0.02-0.3 p/p_0 range.

Scanning Electron Microscopy: SEM was conducted on a FEG microscope (Hitachi SU 5000) at an accelerating voltage of 5 kV, using samples previously sputter-coated with carbon. This microscope is equipped with a Si(Li) EDS detector (AZtec from the Oxford Instruments) with a 60 mm^2 window.

Infrared spectroscopy: FTIR was performed on a Bruker Alpha spectrometer using an attenuated total reflectance (ATR) accessory and a diamond crystal as the reflective element. The spectra were taken at a resolution of 4 cm^{-1} and 128 scans.

Raman spectroscopy: Raman spectra were recorded using a near-IR FT-Raman spectrometer (Bruker RFS 100/S instrument) with a CW Nd:YAG laser (λ_{ex} = 1064nm) as an excitation source. A laser power of 50 mW was used. The spectra were measured in the region 50 – 4000 cm^{-1} with a resolution of 2 cm^{-1} and were accumulated over 1000 scans. For the iodine evolution analysis, the

Raman spectra were taken every one hour for 24 hours, every two hours for the next 24 hours, and every four hours for the last 24 hours (three days spectra collection in total).

Diffuse reflectance UV-vis spectroscopy: The UV-Vis experiments were carried out on a Varian Cary 5000 spectrometer using Praying Mantis™ Diffuse Reflection Accessory adapted for the characterization of powder samples. The spectra were recorded in the 200-800 nm spectral range with a resolution of 1 nm. The diffuse reflectance spectra were plotted using the Kubelka-Munk function.

Electron paramagnetic resonance: The EPR spectra were recorded using a Bruker ELEXYS E580 operating at 9.6 GHz. All spectra were recorded at room temperature with respectively 1G for modulation amplitude and 5mW for microwave power. In situ irradiation of samples were performed with an LC8 Hamamatsu irradiation lamp using the full spectrum

Band gap evaluation: The apparent band gap energy (E_g) of the materials was evaluated using the data obtained by diffuse reflectance UV-vis spectroscopy. E_g was estimated by the Tauc plot [22] of the so-called Kubelka-Munk function [23] $[(F(R)h\nu)^n]$ against the photon energy ($h\nu$), where h is the Planck constant (4.14×10^{-15} eV.s), ν is the photon frequency (Hz), and $F(R)$ is defined as below (Equation (1)). The index n is dependent on the electron transition observed in the examined material – e.g., indirect allowed transition (n = 1/2), direct allowed transition (n = 2), indirect forbidden transition (n = 3), or direct forbidden transition (n = 2/3). As UiO-66 compounds are reported to present a direct band gap, these calculations were carried out considering n = 2 [24,25]. $F(R)$ was calculated by Equation (1), where R is the reflectance (%) assessed by UV-vis spectroscopy.

$$F(R) = \frac{(1-R)^2}{2R} \quad (1)$$

The energy values from the valence band (E_{VB}) and from the conduction band (E_{CB}) were obtained by the Nethercot expressions [26] according to Equations (2) and (3), respectively. Here, E_e is the energy of free electrons in the hydrogen scale with a fixed value of 4.5 eV vs. SHE (Standard Hydrogen Electrode), and X is the geometric mean of the Mulliken electronegativity (arithmetic mean between the electron affinity and the first ionization energy of an atom) of the constituent atoms in the semiconductor [27].

$$E_{VB} = X - E_e + 0.5E_g \quad (2)$$

$$E_{CB} = E_{VB} - E_g \quad (3)$$

2.3 IODINE ADSORPTION TESTS IN UIO-66

Adsorption kinetics: A home-made filtration bench supplied with non-radioactive iodine (^{127}I) was used in order to evaluate the evolution of iodine content trapped within MOF materials (see Figure S2). Briefly, the gaseous iodine is generated using a permeation oven (VICI Metronics Dynacalibrator® Model 150) heated to 100 °C and containing permeation tubes with solid-state iodine crystals. This heating allows the sublimation of iodine and its vapors (0.8 $mg.h^{-1}$) are entrained by an argon flow at a flow rate of 10 $L.h^{-1}$, controlled by a flowmeter (Bronkhorst High-tech E-Flow), providing an iodine concentration of 0.08 $mg.L^{-1}$. Then, the gas flow reaches a filtration cell which contains a frit of porosity 2, adapted to the width of the tube (4 mm). The MOF powdered sample is placed over the frit, allowing the gaseous iodine to pass through it at room temperature. The amount of I_2 that have not been trapped within the MOF is captured in a two-liter bottle, filled with a 0.1 M potassium iodide solution. This solution makes it possible to chemically transform the I_2 into I_3^- according to the Equation (4).

$$I_2 + I^- \leftrightarrow I_3^- \quad (4)$$

Magnetic stirring is applied to ensure constant agitation and homogeneity of the solution. Using a peristaltic pump (Cole-Parmer Masterflex L/S Model 77201-60), the I_3^- solution is continuously dosed by a Shimadzu UV1800 UV-vis spectrometer. In parallel, a blank solution of KI (0.1 M) is pumped into the spectrometer in order to have a continuous reference. The wavelength is set to 352 nm during the analysis, which corresponds to one of the adsorption bands of the I_3^- aqueous species. UV-vis measurements are then collected every four minutes over a period of 16 hours. For each sample analyzed, two measurements are realized: the first corresponds to a blank that is applied in order to obtain the iodine flux delivered by the assembly during the experiment without filter solid; the second is the actual test carried out in the presence of a MOF sample. Once the two measurements are done, the difference between them generates a third curve, which corresponds to the theoretical absorbance associated with the iodine trapped inside the pores of the MOF. Thanks to a preliminary calibration, it is possible to measure the mass of iodine trapped per quantity of MOF.

The kinetics of adsorption for the different UiO-66 materials was evaluated using the Linear Driving Force (LDF) model [28], which was already successfully applied in very similar systems containing UiO-66 and I_2 [29]. The LDF model is represented by the Equation (5), where *F(t)* is the fractional uptake ($m_t/m_{t\,=\,16\,h}$) – m_t is the uptake mass at a given time and $m_{t\,=\,16\,h}$ is the uptake mass at t = 16 h –, k_{LDF} is the effective mass transfer coefficient (h^{-1}) at given temperature and pressure (in this case, room temperature and ambient pressure), and *t* is the time in hours.

$$\mathrm{F(t)} = 1 - e^{-k_{LDF}\,t} \tag{5}$$

Chemometrics: Chemometric analysis was carried out on the Raman spectra obtained during the course of the iodine sorption using the Multivariate Curve Resolution-Alternating Least Squares (MCR-ALS) algorithm [30]. The experimental data matrix (D) was obtained by loading the Raman

spectra of the I_2@MOFs. The number of components of the system was evaluated by the Singular Value Decomposition (SVD) algorithm. The initial estimation of the factor matrix was obtained by the Evolving Factor Analysis (EFA). Non-negativity constraints were applied to all species of the spectra (S^T) and concentrations (C) matrices by using the fast non-negative least squares (fnnls) algorithm [30]. Unimodality constraints were also imposed to all species of the concentrations matrix (C) based on the same algorithm. The spectra were divided by the Euclidean norm, the maximum number of interactions was set to 500 and the convergence criterion to 0.1.

3. RESULTS AND DISCUSSION

3.1 STRUCTURAL CHARACTERIZATION

The weight percentage (wt.%) of hafnium and zirconium in the synthesized UiO-66 were assessed by ICP-EOS and the results are displayed in Table 1, alongside to the atomic percentages of metal constituents (at.%) calculated through the elemental ratio Hf/Zr. The UiO-66(Zr) and UiO-66(Hf) exhibited 100 at.% Zr and 100 at.% Hf, respectively. The intermediate samples – UiO-66(Hf/Zr = 1:3), UiO-66(Hf/Zr = 1:1) and UiO-66(Hf/Zr = 3:1) – exhibited 25 at.% Hf, 51 at.% Hf and 75 at.% Hf, respectively. For such reason, in order to simplify the notation of the mixed UiO-66(Hf/Zr), they were named according to their various amounts of Hf – i.e., UiO-66(25% Hf), UiO-66(51% Hf) and UiO-66(75% Hf), hereafter. These values are exactly, or very close (in the case of UiO-66(51% Hf)), to the initial ratio of precursors during the synthesis, demonstrating that they were well accomplished.

The SEM images of the UiO-66 products synthesized in this work are displayed in Figure 1. They show crystals morphology of typical aggregates of octahedral shapes in agreement with that expected for UiO-66 samples from literature [12]. The EDS/elemental mapping image of UiO-66(Hf/Zr 1:1) reveals that Zr and Hf atoms are homogeneously dispersed throughout the

crystallites. This observation is also verified by the EDS/elemental mapping of the other compounds with different Hf/Zr ratios (see Figure S3). Moreover, the elemental ratios of hafnium and zirconium obtained by EDS are close to those obtained by ICP-EOS (see Table 1), showing that the crystals have a similar composition to that of the bulk powdered sample.

In this work, the UiO-66 compounds exhibited crystallites ranging from 100 nm to 3.3 µm (Figures 1 and S2). This difference is also dependent on the Hf/Zr atomic ratio, since the presence of hafnium seemed to induce the growth of bigger crystals. Aiming to emphasize this variation, the particle size distribution of the crystallites is presented in Figure S4. While UiO-66(Zr) present crystallites ranging between 100 and 250 nm, UiO-66(Hf) can lead to crystallites up to 3.33 µm (Figure S3 and Table 1).

Figure 2 shows powder XRD patterns of UiO-66 compounds after activation with various Hf/Zr ratio and also the evolution of the lattice parameter *a* of the cubic cell. Typical diffraction Bragg peaks of the UiO-66 structure were observed at 2θ about 7.4º, 8.5º, 12.0º, 14.1º, 14.8º, 17.1º, 18.6º, 19.1º, 21.0º, 22.3º, 24.2º, and 25.8º, which have been attributed to its (111), (200), (022), (113), (222), (004), (133), (024), (115), (044), (135) and (006) crystal planes, respectively [31]. Lattice parameters were refined by Le Bail analysis method using the JANA software [32]. UiO-66 topology possesses a FCC cell, where the lattice parameter *a* was found to be a function of the Hf/Zr atomic ratio, going from *a* = 20.7696(8) Å in UiO-66(Zr) down to *a* = 20.7232(7) Å in UiO-66(Hf) (Table 1). It is worth mentioning that those values, as well as their variation, are in good agreement with those reported in other studies [12,14]. This is ascribed to the fact that Zr^{4+} and Hf^{4+} cations have a very similar ionic radius – 0.84 Å (Zr^{4+}) and 0.83 Å (Hf^{4+}) for environment coordination of VIII – [33] and, at the same time, the Hf^{4+} is known to present a higher electronegativity than the Zr^{4+} (0.96 against 0.90) [34]. Therefore, the higher acid character of Hf^{4+} contributes to decrease the size of the Hf–O bonds when comparing to the Zr–O bonds [34,35]. Moreover, we observed the presence of a single (111) peak at different Hf/Zr ratios, which reflects

a solid solution of $Zr_{6-x}Hf_x$ type within UiO-66 crystals, as confirmed by the EDS cartography (Figure 1). If one considers the segregation of two pure phases related to different amounts of UiO-66(Zr) and UiO-66(Hf) solids, a doublet of Bragg peaks should be visible instead.

Diffuse reflectance UV-vis spectroscopy was performed in order to evaluate the metal influence on the optic properties of the UiO-66(Zr:Hf) materials synthesized here (Figure 3a). The spectrum of pristine UiO-66(Zr) shows only absorptions in the UV domain, at 242 nm with a shoulder at 292 nm (Figure 3a). This band is attributed to linker-based HOCO (Highest Occupied Crystalline Orbital) to LUCO (Lowest Unoccupied Crystalline Orbital) transitions, as the binding energy of the zirconium d-orbitals is too low and prevents the overlap with the π^* orbital of the BDC organic linker [36]. Then, it is observed that the relative intensity of the shoulder contribution at 292 nm increases progressively with the hafnium content to finally give rise to a broad band shifting to around 240-300 nm. (Figure 3a). Since the change in the intensity of this transition is not accompanied by a variation of its energy (there is no wavelength shift), this phenomena is ascribed to the different molar extinction coefficient of zirconium and hafnium [37]. The band gaps of the UiO-66(Zr:Hf) compounds were extracted from the Tauc plot [22] using the Kubelka-Munk [23] function and are exhibited in Table 1, alongside the respective E_{VB} and E_{CB} values. The incorporation of hafnium has a significant influence over the band gap of the samples (Figure 3b and Table 1). The E_g reduces from 4.07 eV in UiO-66(Zr) down to 3.98 eV in UiO-66(Hf). It is worth mentioning that the value obtained for UiO-66(Zr) is in agreement with the literature [13]; however, this happens to be the first time that experimental data is acquired for UiO-66(Hf) [24]. Although Yang *et al.* [24] demonstrated that there is an underestimation of the band gap energies for UiO compounds when E_g is calculated by density functional theory (DFT), an operation applied to their DFT results allowed them to predict values that correspond exactly to the experimental data obtained elsewhere for UiO-66(Zr) (4.07 eV) [13] and UiO-67(Zr) (3.68 eV) [38]. Nevertheless, this method found the value of 3.74 eV for UiO-66(Hf), which is significantly different from the 3.98 eV obtained in this work.

Figure 4 displays the nitrogen gas sorption isotherms collected for the series of UiO-66(Zr:Hf). All the compounds present a type-I isotherm according to IUPAC classification, which is characteristic of microporous materials (Table 1) [39]. One can see that the incorporation of hafnium in UiO-66(Zr) compound has a drastic effect over the Specific Surface Areas (SSAs) of the samples calculated by the BET method. When replacing zirconium atoms by hafnium in the UiO-66 structure, the SSA decreases from 1262(33) $m^2.g^{-1}$ for UiO-66(Zr) to 818(24) $m^2.g^{-1}$ for UiO-66(Hf). It stays in between for the other Hf/Zr ratios: 1016(29) $m^2.g^{-1}$ for UiO-66(25% Hf), 980(25) $m^2.g^{-1}$ for UiO-66(51% Hf), and 898(26) $m^2.g^{-1}$ for UiO-66(75% Hf) (Table 1). The same behavior is observed for the microporous volume of the samples, which decreases from 0.598(8) $cm^3.g^{-1}$ in UiO-66(Zr) to 0.408(9) $cm^3.g^{-1}$ in UiO-66(Hf) (Table 1). The results are in agreement with others reported in the literature and they are coherent with the atomic mass of hafnium (178.49 u) and zirconium (91.224 u) [12,40]. Inarguably – since those values are normalized to a mass unity (g^{-1}) – when considering an isostructural UiO-66 solid, the presence of a heavier metal that densifies the material will reduce its SSA and its specific microporous volume. However, this is not to be related to the actual surface or microporous volume per molar unit, as the materials synthesized here present the same pore structure. For this reason, in order to facilitate the comparison between these values for different metals, the SSA and the specific microporous volume were normalized to the molecular weight of UiO-66 – in other words, they are also presented as a function of molar quantities (mol^{-1}) in Table 1.

Aiming to investigate the influence of the metal Hf/Zr substitution on the chemical bonds of the UiO-66 compounds, FTIR and Raman spectroscopies were conducted. The Raman spectra are displayed in Figure 5 and are normalized to the band at 1618 cm^{-1} (C–O asymmetric stretching), while the FTIR spectra, displayed in Figure 6, are normalized to the band at 1392 cm^{-1} (C=C–(COO) asymmetric stretching). These bands were chosen since they are not affected by the metal Hf/Zr substitution. The vibrational frequency of the main FTIR and Raman bands are presented in

Table 2 alongside their assignment. The attribution of the bands resulted from the animations of vibrational modes of a hydroxylated UiO-66(Zr) that were calculated by Valenzano *et. al.*, [13] and are available at the CRYSTAL Web site: https://www.crystal.unito.it/vibs/uio66_hydro/.

The evolution of the Raman spectra as a function of the Hf/Zr ratio is presented in Figure 5. The spectra exhibit clearly the development of a new band centered at 181 cm^{-1}, which is tentatively assigned to linker to metal-cluster in-plane bending + μ_3–O bending (μ_3– stands for an element which is connected to three metals) [13]. Moreover, blue-shift effects are observed when hafnium content increases in the bands at 238, 500, 1431, and 1449 cm^{-1}. The first blue-shifted band, at 238 cm^{-1}, relates to two vibrational modes: linker to metal-cluster out of plane bending and M–(OH)–M bending (M = Zr, Hf; Figure S5a); whereas the second one, at 500 cm^{-1}, is related to the μ_3-O and μ_3-OH in-phase bending (cluster breathing) [13] (Figure S5b). In addition, the bands at 209 and 231 cm^{-1} are ascribed to the O–C–O translation mode and they are only present in UiO-66(Zr) and in UiO-66(Hf) Raman spectra, respectively (Figure 5) [13]. Another band, at 1431 cm^{-1}, is related to two vibrational modes: in-plane asymmetric (C=C)–H bending + asymmetric C=C stretching [13]. Finally, the last one, at 1449 cm^{-1}, is associated to the C–C symmetric stretching [13] (Figure S5c).

In order to get complementary information about the metal influence on the vibrational behavior of the UiO-66 compounds, FTIR spectroscopy was also applied to these samples. As observed in the Raman spectra, the five FTIR bands at 554, 679, 702, 729, and 3675 cm^{-1} also shift toward higher wavenumbers with the increase of the hafnium content (Figure 6). The first two, at 554 and 679 cm^{-1} are related to the M–(OC) asymmetric stretching (Figure S6a) and to the μ_3–O stretching (Figure S6b), respectively [13]. The band at 702 cm^{-1} is influenced by three modes of vibration: μ_3–OH bending + O–C–O bending + C=C–(COO) bending, while the one at 729 cm^{-1} corresponds to the aromatic ring torsion mode (Figure S6b) [13]. The last one, at 3675 cm^{-1}, is related to the OH stretching mode (Figure S6c) [13]. Moreover, it is interesting to note that the relative intensity of the bands at 448 and 474 cm^{-1} dramatically depends on the Hf/Zr atomic ratio (Figure 6): a higher

content of hafnium favors the band at 448 cm^{-1} (antiphase μ_3–OH stretching), whereas higher content of zirconium leads to an increase of the one at 474 cm^{-1} (in-phase μ_3–OH stretching) [13].

The presence of blue-shifts in the FTIR and Raman bands implies that these vibrational modes require higher energy in UiO-66(Hf) than in UiO-66(Zr). Studies have shown that the average μ_3–(O,OH) bond is shorter in UiO-66(Hf) (2.102(17) Å) than in UiO-66(Zr) (2.233(1) Å) [12,14]. An identical trend is also observed for the M–(OC): Hf–(OC) = 2.086(8) Å and Zr–(OC) = 2.107(2) Å (OC = oxygen from carboxyl group) [12,14]. However, the opposite was found for the O–C bond (from bidentate carboxylate group): 1.304(21) Å in UiO-66(Hf) against 1.256(2) Å in UiO-66(Zr) [12,14]. These distance variations are all consistent with the higher acidity of Hf^{4+} compared to that of Zr^{+4}, which increases the interaction between the metallic cation, the oxo, the hydroxyl, and the oxygen from carboxyl groups within the hexanuclear $[M_6O_4(OH)_4]$ core, inducing a stiffening of the interatomic bonding in UiO-66(Hf) [34,41]. Therefore, it explains the blue-shifts regarding the μ_3–O, the μ_3–OH, and the M–(OC) species. The other blue-shifts, related to the aromatic part of the material, are ascribed to the smaller cubic lattice parameter of UiO-66(Hf), which induces a structural shrinkage of the organic linker and therefore, the shortening of the associated chemical bonds.

3.2 IODINE EVOLUTION WITHIN UiO-66 POROUS STRUCTURE

In order to investigate the possible influence of the metal, the powdered samples UiO-66(Hf), UiO-66(75% Hf), UiO-66(51% Hf), UiO-66(25% Hf) and UiO-66(Zr) have been exposed to gaseous iodine flow for 1 hour or 16 hours. The glass cell used to capture iodine (see Figure S2) was prepared and sealed inside a glovebox under argon atmosphere, which avoided the contact of the powder with atmospheric water. At first, their kinetic iodine sorption curves were obtained and are presented in Figure 7. Even though early stages (1-2 h) of the adsorption process on UiO-66(Hf) and UiO-66(Zr) seem to lead to an equivalent amount of iodine trapped by the UiO-66

pores (76 $g.mol^{-1}_{(UiO-66)}$ = 0.30 I_2 molecules per unit of UiO-66), the presence of hafnium significantly enhances the adsorbed iodine amounts from contact times longer than two hours. This feature put forward possibility that two different adsorption processes exist within the UiO-66 cavities. The first one could occur regardless the metal nature of the inorganic core, whereas in the second step, the presence of hafnium seems to favorize the increase of adsorbed iodine content. Different adsorption sites for I_2 within UiO-66(Hf) structure were already reported in the literature depending on the presence of defects on its structure [42]. Here, after 16h contact with the gaseous iodine stream, the UiO-66(Hf) phase was able to adsorb 285 g of I_2 per mol of UiO-66 (approximately 1.12 I_2 molecules per unit cell of UiO-66), whereas UiO-66(Zr) only captured 230 $g.mol^{-1}_{(UiO-66)}$ (approximately 0.90 I_2 molecules per unit cell of UiO-66). The other three samples – UiO-66(25% Hf), UiO-66(51% Hf), and UiO-66(75% Hf) – stayed in between those values (see Table 1), which confirms the premise that hafnium favors the I_2 capture.

For better understanding the hafnium influence on the I_2 adsorption kinetics, the experimental data of the iodine adsorption in UiO-66 compounds was fitted according to the LDF model (see Figure S7). The effective mass transfer coefficient (k_{LDF}), the correlation coefficient (R^2), and the equilibration time to reach $F(t)$ = 0.90 and $F(t)$ = 0.99 are displayed in Table 3. There is a clear dependence between the k_{LDF} values and the hafnium amount in the UiO-66 structure, where the UiO-66(Hf) exhibits the smallest mass transfer coefficient (0.267(1) h^{-1}), and UiO-66(Zr) the highest (0.323(5) h^{-1}). The other three compounds (UiO-66(25% Hf), UiO-66(51% Hf) and UiO-66(75% Hf)) are in between those values. However, surprisingly, the UiO-66(51% Hf) exhibits a small shift from the expected behavior, since its k_{LDF} value is higher than both UiO-66(25% Hf) and UiO-66(75% Hf) (see Table 3 and Figure S7). Still, this is coherent with the residence time of iodine in the UiO-66 compounds, which goes from 30 min in UiO-66(Hf) to 90 min in UiO-66(Zr), staying in between for UiO-66(25% Hf) (50 min), for UiO-66(51% Hf) (80 min), and for UiO-66(75% Hf) (60 min). Furthermore, although the maximum capacity of iodine adsorption by the materials here evaluated was not achieved in 16 hours, the LDF exponential curve fits quite

well with the experimental data, as verified by the R^2 values between 0.981 and 0.997, except for UiO-66(Zr) which exhibited a slightly smaller R^2 of 0.943. The UiO-66 compounds can achieve $F(t)$ = 0.90 in approximately seven to eight hours. For instance, the UiO-66(Zr) achieves 90% of its total adsorption capacity (considered from a total of 16 hours of contact) in 7 h 8 min whereas, in the same conditions, UiO-66(Hf) took 8 h 37 min. Finally, the UiO-66 compounds with 50% or less of hafnium can take up to 14 h 57 min to achieve 99% of their adsorption capacity. This value rises for hafnium-richer (>50%) UiO-66, with t = 15 h 46 min and t = 17 h 15 min for UiO-66(75% Hf) and UiO-66(Hf), respectively.

At this point, it is worth mentioning that the color of the samples drastically changes after 16 hours of contact with the iodine gaseous stream. Indeed, the white original UiO-66 powders became orange-brown immediately after contact with I_2 but turned yellow after being exposed to the ambient atmosphere for 72 hours (Figure 8). Due to their similar color change, the iodine chemical behavior encapsulated in the three UiO-66 samples was first studied by UV-vis spectroscopy. Figure 8 presents the spectra obtained after leaving the iodine bench and after 72 hours of exposition to the ambient air atmosphere. For comparison purposes the spectra of the pure UiO-66 are also displayed.

After the contact between UiO-66 and iodine, the three I_2@UiO-66 samples showed the same behavior with the presence of two new broad bands maximizing at 292 and 361 nm, in addition to the bands of the UiO-66. These new contributions at 292 and 361 nm reveal the formation of the anionic I_3^- species [43]. However, due to the successive forms of the iodine species after adsorption, this absorption includes probably other contributions in the visible range between 400 and 550 nm. The first one, corresponding to the "isolated" iodine form in gas phase, is expected to be observed at 520 nm due to the allowed $\pi_g^* \rightarrow \sigma_u^*$ transition [44,45]. Additionally, the spectral signature at lower wavelengths (around 400-500 nm) was attributed to charge transfer complexes between the I_2 and the aromatic ring of the BDC linker, since I_2 is well known for forming this

type of interaction with benzene, which presents a high electron donor character [46,47]. Thus, "free" or weakly perturbed iodine molecules are assumed to contribute to the observed absorption around 400-500 nm. Consequently, whatever the metal Hf/Zr nature, the iodine adsorption mechanism within the framework of the UiO-66 series is initiated by the adsorption of "free" I_2 molecules that progressively go through the "perturbed" I_2 moiety and then transformed into I_3^-, which is the most stable species. At this point, it is already possible to deduce that the adsorption that occurs during the first 1-2 h is mainly dominated by "free" I_2 molecules, reason why there is no influence of the Hf/Zr content over the amount of I_2 trapped within the pores of UiO-66 for $t < 2$ h.

Raman experiments were carried out in order to follow the sorption and evolution process of iodine within the three Hf/Zr compositions of the UiO-66 structures. It is worth mentioning that most of the UiO-66 bands keep the same positions after the iodine contact. However, changes can be observed in terms of relative intensity for some bands related to the BDC linker and, when hafnium is present, to the hydroxyl and oxo groups, which will be discussed below. Figure 9 shows the evolution of the Raman spectra of the I_2@UiO-66 compounds after 16 h of exposure in the 50–275 cm^{-1} region, which is characteristic of the iodine species inserted in UiO-66(Zr), UiO-66(51% Hf), and UiO-66(Hf). The spectra were normalized to the band at 1618 cm^{-1}, which is not affected by the iodine adsorption. They all showed the development of three bands centered at 115, 173, and 206 cm^{-1}, while a fourth component is observed at 156 cm^{-1} in I_2@UiO-66(Zr) (Figure 9a), and at 141 cm^{-1} in I_2@UiO-66(51% Hf) and I_2@UiO-66(Hf) (Figure 9b and 9c).

In order to identify the signature of the single iodine species that are present in the Raman spectra and to distinguish the Raman contribution from "free" I_2, "perturbed" I_2, and I_3^-, Multivariate Curve Resolution-Alternating Least Squares (MCR-ALS) algorithm was applied to the Raman experimental data. This method aims to extract relevant information of the single components present in a complex system. By using a bilinear model decomposition of the experimental data into the product of two matrices, MCR-ALS provides the spectra and the concentration peak

profiles corresponding to the single components [30]. The MCR-ALS calculation allowed the extraction of three spectra assumed to correspond to three species: "free I_2", "perturbed I_2", and "I_3^-" (Figure 10). The first one shows mainly a band at 206 cm^{-1}, while the second spectrum displays a broad band at 173 cm^{-1} with a shoulder around 156 cm^{-1}. The third spectrum is characterized by a main band centered typically at 115 cm^{-1} with a shoulder at 141 cm^{-1}. These bands were summarized in Table 4 and their values were compared to other reported in the literature, which allowed the identification of these three species.

Due to the close proximity between the band observed at 206 cm^{-1} and that reported for isolated iodine in gas phase (210 cm^{-1}), the 206 cm^{-1} vibration was assigned to the symmetric stretching of the I_2 molecule assumed to be trapped in the porous volume of the MOF, in the absence of strong interaction with its walls [48]. The progressive appearance of contributions at about 173 and 150 cm^{-1}, concomitantly to the reduction of the 206 cm^{-1} band, was attributed to the interaction between the I_2 and the UiO-66. This intermediary state, which is associated to the perturbed iodine, presents lower wavenumbers than the crystalline I_2 solid (180 – 188 cm^{-1}) [49]. This is ascribed to the presence of strong electron donor molecules – in this case, the aromatic ring from the BDC linker – that induces a decrease on the frequency of these vibrational modes [50]. This species is defined as "perturbed" iodine, due to a charge transfer complex that may generate different polynuclear iodine species of I_n^{-1} type (n = 3, 5, 7, …) [51]. Finally, the band centered at 115 cm^{-1}, which is observed in the third extracted spectrum, is attributed to I_3^- and corresponds to the final stable state. It is worth mentioning that this assignment is definitely confirmed by the MCR-ALS approach, with the extraction of two contributions relative to the symmetric stretching of the I_3^- molecule (115 cm^{-1}) and to its asymmetric stretching, which presents higher energy (141 cm^{-1}) [52]. Even though the asymmetric stretching (141 cm^{-1}) of the I_3^- is not supposed to be active in Raman spectroscopy, the specific environment of such molecule or its confinement inside the UiO-66 framework induces a small deformation on its structure. At that point, due to the lowering of its symmetry, this vibrational mode becomes optically active [53]. In addition, the spectrum assigned to

perturbed I_2 also shows a band at around 156 cm^{-1} as a shoulder of the main band observed at 173 cm^{-1}; this feature is particularly observable in the case of I_2@UiO-66(Zr). This shoulder may be assigned to successive evolution stage of the perturbed iodine, probably superimposed with the residual contribution of the asymmetric stretching of I_3^-, which cannot be resolved by the MCR procedure [51,52]. Therefore, despite the complexity of the iodine species within the framework of UiO-66 materials, this works focuses on the contribution of the progressive evolution from the most currently reported ones: "free" I_2, "perturbed" I_2, and I_3^- [54].

The evolution and the relative intensity of these bands in Raman spectra (Figure 9) were found to be dependent on the Hf/Zr atomic ratio. The first spectra recorded after the 16h iodine exposure procedure show that the relative intensity of the 206 cm^{-1} band is much higher for I_2@UiO-66(Zr) (Figure 9a) than for I_2@UiO-66(Hf) (Figure 9c). The intensity of this band gradually decreases with time to the benefit of another at 173 cm^{-1} and also at 156 cm^{-1}, which becomes clearly observable. Then, the other band intensity at 115 cm^{-1} starts to increase. This finding reinforces the idea that the "free" I_2 trapped within the UiO-66 pores was slowly transformed into "perturbed" iodine and then, into I_3^-, in agreement with the UV-vis results (Figure 8). However, this transformation did not follow the same kinetics in I_2@UiO-66(51% Hf) and in I_2@UiO-66(Hf). Indeed, contrary to what was observed in I_2@UiO-66(Zr), the band at 206 cm^{-1} is almost unperceptive in the Hf-containing UiO-66 compounds since the beginning of the analysis (t = 30 min). In these cases, the most intense band at t = 30 min is the one at 173 cm^{-1}, suggesting that the transformation from the "free" I_2 into "perturbed" I_2 had already occurred during the passage of the gaseous iodine stream. Moreover, it is interesting to note that the asymmetric I_3^- stretching at 141 cm^{-1} is clearly observed with I_2@UiO-66(51% Hf) and I_2@UiO-66(Hf) since the first hours of analysis, whereas this contribution is overlapped by the broad band at 156 cm^{-1} in I_2@UiO-66(Zr) and never observed, even after 72 hours. In addition, the higher intensities of the normalized bands at 206, 173, and 115 cm^{-1} highlight the dramatic influence of hafnium on the spectral concentrations of the iodine species. Indeed, high I_3^- contents are observed from shorter times (1-3

hours) and remain at a magnitude order of intensity of about five times for UiO-66(51% Hf) and nine times for UiO-66(Hf), compared to that of UiO-66(Zr) (see Figure 11). Therefore, these results tend to demonstrate the more efficient and faster I_2 to I_3^- transformation in the presence of hafnium. In fact, the slow I_2 to I_3^- conversion in the case of UiO-66(Zr) creates a lot of I_n^- intermediate species (at about 150 cm^{-1}). However, when hafnium is present, the I_2 to I_3^- evolution occurs in such a time scale that these intermediates are not visible in the Raman spectra – this feature is highlighted by the absence of the band related to the I_n^- species at about 156 cm^{-1}.

In order to emphasize this point, the higher normalized intensities achieved for the bands at 173 and 115 cm^{-1} were plotted as a function of the Hf/Zr atomic ratio and are presented in Figure S8. Aiming to confirm the results of the samples that have been in contact with the gaseous iodine for 16 hours, a comparison was also performed with the UiO-66 compounds in contact with the I_2 gas stream for only one hour. Although the signal/noise ratio of these spectra was relatively low due to weaker sorption rate (i.e., lower trapped iodine content within the UiO-66 pore) compared to the 16h iodine exposure, the trend reported in Figure S8 is similar for both bands and shows an increase of the spectral concentration of the iodine species with the hafnium content. This confirms that I_2@UiO-66(Hf) has the higher capacity to trap iodine within its pores and this uptake decreases together with the hafnium amount in the UiO-66 framework, which is in total agreement with the adsorption kinetic measurements (Figure 7).

Intending to obtain a systematic comparison for the iodine uptake and for the conversion kinetics as a function of hafnium content, the normalized intensities of the bands at 115 and 173 cm^{-1} (corresponding to adsorbed iodine and I_3^-, respectively) were plotted against time and are presented in Figure 11a. The corresponding instantaneous rate obtained from the first order derivative is reported in Figure 11b. The evolution of the bands at 115 and 173 cm^{-1} and their first order derivative confirms that the Hf/Zr atomic ratio influences the transformation of I_2 into I_3^- (Figure 11). The I_2@UiO-66(Hf) exhibits the fastest transformation as confirmed by its first order

derivative (Figure 11b) and the highest Raman intensity plateau among all the materials, which suggests that it also captured more iodine than UiO-66(51% Hf) and UiO-66(Zr). In this case, the I_3^- highest signal was obtained after 4h, and the lowest I_2 signal after 24h. The I_2@UiO-66(51% Hf) presented an intermediate kinetic of iodine evolution. However, even though its uptake capacity is lower than I_2@UiO-66(Hf), the maximum I_3^- and minimum I_2 intensities were also reached after 4 and 24h, respectively. Finally, the I_2@UiO-66(Zr) had the lowest kinetic transformation and captured less iodine than the others. It reached the I_3^- and I_2 plateaus after 3 and 18h, respectively. These results agree with the adsorption kinetic measurements (Figure 7).

Aiming to obtain additional information on the interaction of iodine with the UiO-66 framework, the spectral study was continued by coupling the Raman study with FTIR analysis and focusing on the vibrational modes of the lattice perturbed by the iodine species above 400 cm^{-1}. The FTIR and the Raman spectra of the three pristine samples – UiO-66(Zr), UiO-66(51% Hf) and UiO-66(Hf) – and after the iodine contact under ambient air for 30 minutes and 72 hours are presented in Figure 12. Firstly, considering the FTIR spectra (Figure 12a), two different behaviors are observed in the 400-500 and 650-750 cm^{-1} regions depending on the nature of the metal Hf/Zr. In UiO-66(Zr), the relative intensity ratio ($I_{\lambda 1}$/ $I_{\lambda 2}$) of the bands at 729 and 743 cm^{-1} (I_{729}/I_{743}) decreases after 30 min and increases again after 72 h, reaching the initial intensity ratio of the pristine MOF. On the other hand, in pristine UiO-66(Hf), the band at 735 cm^{-1} progressively decreases in favor of a band at 745 cm^{-1}, which is the only one observed after 72 h of analysis. Since the bands at 729 – 735 cm^{-1} are related to the aromatic ring torsion mode, the spectral change indicates that the I_2 molecules interact with this part of the UiO-66 during its evolution, regardless of the nature of the metal that is present in the structure. This finding is in agreement with the charge transfer complexes between the I_2 and the aromatic ring of the BDC linker [46,47]. Moreover, the spectra recorded for I_2@UiO-66(Hf) show the development of a new band at 675 cm^{-1}, at the same time that the relative intensity of the band at 443 cm^{-1} decrease when comparing to the pyridine UiO-66(Hf) spectrum. This evolution is not observed for UiO-66(Zr), while the

UiO-66(51% Hf) presents an intermediate behavior between the UiO-66(Zr) and the UiO-66(Hf). These bands, at 675 and 443 – 446 cm^{-1}, are related to the μ_3–O stretching and μ_3–OH antiphase stretching, respectively. This finding suggests that the oxo and hydroxyl groups have an influence over the iodine transformation within the UiO-66 structure when hafnium is present. Considering the Raman spectra (Figure 12b), differences are also noticed right after the end of I_2 exposure (t + 30 min) and after 72 hours for the bands at about 1144, 1433, and 1452 cm^{-1} in UiO-66(Hf), whereas these modes are very weakly perturbed in UiO-66(Zr). It is worth mentioning that these bands are attributed to organic linker vibrations (see Table 2). No changes related to the metal Hf/Zr inorganic polyoxo/hydroxo cluster vibrational modes were identified in the Raman spectra after the iodine contact. Note also that the linker-related aromatic CH stretching in the 3050-3080 cm^{-1} spectral range are also much more perturbed in the presence of iodine in UiO-66(Hf) than in UiO-66(Zr) (Figure S9).

Since the substitution of zirconium by hafnium induces clear spectral change in the Raman/FTIR spectra and leads to significant changes in the I_2 adsorption process (kinetic of reaction and nature of stable species), the role of these metallic centers was further investigated using EPR to determine whether a redox mechanism involving the cation (Zr^{4+} or Hf^{4+}) was associated with the I_2 capture by UiO-66. Aiming to detect and to enhance such redox process, the I_2@UiO-66(Zr) and I_2@UiO-66(Hf) were irradiated after the exposure to iodine, as presented in Figure 13. The spectra reveal that the metallic cations (Zr^{4+} and Hf^{4+}) are not reduced to its trivalent state during the I_2 adsorption and transformation to I_3^-, as shown by the absence of a signal at $g < 2$. Effectively as the g matrix is governed by the electronic structure of the transition metal, if reduction of Hf^{4+} and Zr^{4+} occurs, it must result in Hf^{3+} and Zr^{3+}, which exhibits a d^1 electronic configuration that corresponds to a g value below $g = 2$ [55,56]. The EPR spectra obtained after I_2@UiO-66(Hf) irradiation show a small peak centered at $g = 2.01217$ (Figure 13b) and a second peak at $g = 2.00230$ that develop through the irradiation time. The former signal could correspond to an unpaired electron located over an oxygen atom, while the latter signal is assigned to a free

electron. When the irradiation of the I_2@UiO-66 sample is cut off, both signals remain with lower intensity. It is worth noting that, although the irradiation of I_2@UiO-66(Zr) induces the formation of both signals, the peak at g = 2.00230 is very weak compared to that of I_2@UiO-66(Hf). This result could be related to the larger amount of I_3^- stabilized in the pores of I_2@UiO-66(Hf), as revealed by Raman spectroscopy (Figures 9 and 11). In fact, the presence of higher amount of I_3^- is associated with the formation of more unpaired electrons in the course of the $I_2 \rightarrow I_3^-$ transformation. Furthermore, Miyajima *et al.* evaluated the interaction between iodine and aromatic compounds present in coal tar pitches by EPR [57]. They verified that the charge transfer complexes between iodine and aromatic compounds having a π-conjugated system produce an EPR signal – very similar to that obtained in this work – that is related to the presence of organic cation radicals [57]. These statements reveal that the reaction mechanism between UiO-66 and I_2 only involves the organic part of the framework and is not influenced by a redox phenomenon of the metal sites.

To sum it up, the influence of the oxo and hydroxyl groups on the iodine evolution within UiO-66(Hf) structure (Figure 12a) agrees with the higher acid character of hafnium compared to zirconium [13,34,35]. Actually, in UiO-66(Hf), the shrinkage of the μ_3–O and M–(OC) bonds combined with the increase on the length of the O–C bond impoverishes the electronic cloud on the carboxylate group [34,41]. Then, aiming to neutralize this disparity, the electronic cloud from the aromatic ring is delocalized towards the carboxylate. This effect enriches the electron density on the oxo and hydroxyl groups, which affects their vibrational modes (Figure 12a). This phenomenon, coupled with the slightly lower band gap of Hf-based UiO-66 (Figure 3 and Table 1), may also explain the different I_2 loading (Figure 7 and Table 1) and kinetic behavior (Figure 11) in both samples. Indeed, when a semiconductor is irradiated, photons that have energy greater than or equal to the band gap of that material can excite electrons from the valence band (VB) to the conduction band (CB). In this process, when an electron (e^-) jumps into the CB, it leaves a hole (h^+) in the VB, which is considered as a positive charge [58]. Although these entities have

relatively low lifetimes and can annihilate themselves by recombining due to electrostatic interactions, this effect is reduced for materials with low mobility of charge carriers (electrons and holes) [59]. In this scenario, some materials can trap the produced electrons, the holes, or both [60]. Since UiO-66 compounds present a pure linker-based transition [36], both the electrons and holes are created in the aromatic part of the UiO-66 network, which is confirmed by the absence of a redox phenomenon on the metal site – as demonstrated by EPR – and can be related to the low binding energy of the d^0 orbitals of Zr^{4+} and Hf^{4+} [36]. However, due to the higher delocalization of the electronic cloud from the BDC linker towards the inorganic cluster in UiO-66(Hf), the electron-hole recombination is expected to be more difficult, which favors the formation of I_3^- and, consequently, its adsorption on the aromatic ring.

These features allowed the proposition of a model for the transformation mechanism of I_2 to I_3^- in the pores of UiO-66, which is presented in Figure 14. In this case, the entire mechanism is based on the formation of an electron-hole pair in the BDC linker, as represented by the electron donor-acceptor (EDA) complex between the BDC linker and the I_2 gaseous molecule, which should by favored by the smaller band gap of UiO-66(Hf) when comparing to that of UiO-66(Zr). Here, it is worth mentioning that the connection between organic and solid-state chemistry is still not highly developed in the case of MOFs. As reported by Mancuso *et al.*, [61] MOFs can present characteristics of both a solid with a well-defined boundary and also of an infinite quasi-molecule. According to Kolobov *et al.*, [62] this creates some unusual mixed concepts between coordination chemistry (i.e., linker to metal charge transfer, LMCT) and semiconductors physics (band gap structure) in the MOF literature. From this perspective, one must keep in mind that the proposed model for the mechanism in this work only represents a monomolecular interaction between the BDC linker and I_2 molecules. When the entire crystalline structure of UiO-66 is taken into account, the unpaired electron created in the aromatic ring should be able to move through the MOF network. In fact, the EPR signal at $g = 2.01217$ (related to an unpaired electron located over an oxygen atom), suggests that the electron can move over the UiO-66 lattice through the oxygens

present in the inorganic $[M_6O_4(OH)_4]$ (M = Zr, Hf) cluster. Also, when considering the entire UiO-66 lattice, the formation of the electron-hole pair can occur in different linkers, which would help to avoid the recombination process. For instance, Santiago Portillo *et al*. evaluated the lifetimes of photoinduced states in a NH_2-UiO-66(Zr/Ti) material by transient absorption spectroscopy (TAS) and concluded that the bleaching of the ground state are related to a combination of triplet excited states and trapped electrons, which can live up to 25 μs after the lase pulse, demonstrating the relative short life-times of these entities [63]. That being said, the next steps of the mechanism can be easily described by a monomolecular approach in which through the proximity and subsequent polarization of a gaseous iodine molecule by the aromatic ring of the BDC linker, the excited electron jumps from the BDC conduction band (HOCO, π*) to the conduction band of the I_2 molecule (LUMO, σ^*_{5p}), forming an intermediate radical species: $I_2^{\bullet-}$. Then, the radical iodine species can react with another $I_2^{\bullet-}$ to form I_3^- and I^- – which was already described elsewhere for a system composed by iodine in acetonitrile solution [43]. At this point, it is worth mentioning that the EPR spectrum of iodine ions and radicals are hardly observed at room temperature due to the enormous anisotropy of their *g*-factor and to the fast electron spin relaxation that is caused by the large spin-orbit interaction of the iodine atom [57]. For this reason, no signal was observed for the I^- and $I_2^{\bullet-}$ species in the EPR measurements (Figure 13). Finally, the recently formed I_3^- is further stabilized in UiO-66(Hf) than in UiO-66(Zr) due to the higher acidity of Hf^{4+} compared to that of Zr^{4+}, which is also responsible for the smaller lattice parameter of UiO-66(Hf) (*a* = 20.7232(7) Å against *a* = 20.7696(8) Å in UiO-66(Zr)). The enhanced I_3^- stabilization in UiO-66(Hf) should be ascribed to the higher delocalization of the electronic cloud towards the carboxylate group in the presence of hafnium [34,41], which is caused by the shrinkage of the M–(OC) bond (Hf–(OC) = 2.086(8) Å and Zr–(OC) = 2.107(2) Å) [12,14] and by the increase on the length of the O–C bond (UiO-66(Hf): 1.304(21) Å; UiO-66(Zr): 1.256(2) Å) [12,14]. This feature impoverishes the electronic density in the aromatic cycle of the BDC linker, which further stabilizes the $BDC^{\bullet+}$ radical and improve its interaction with the I_3^- species.

To sum it up, the smaller band gap of hafnium favors the EDA complex between the BDC linker and the I_2 molecule, at the same time that the higher acidity of Hf^{4+} favors the I_3^- stabilization and adsorption on the aromatic ring of the $BDC^{\bullet+}$. Since the intermediate iodine species (I^- and $I_2^{\bullet-}$) were not identified in this work by the characterization techniques that were employed, further studies must be conducted in order to detect such species in I_2@UiO-66 systems. In this case, time-resolved spectroscopies and spin-trapping EPR using dimethyl sulfoxide (DMSO) may be valuable tools for evaluating such hypothesis [43,64].

4. CONCLUSIONS

In this work, a series of UiO-66 with different Hf/Zr metal ratios was successfully synthesized and thoroughly characterized before assessing their ability to capture iodine. Characterization shows that crystallites are slightly larger at higher hafnium contents and that the BET specific surface area, lattice parameters and band gap decrease from UiO-66(Zr) to UiO-66(Hf). The substitution of zirconium by hafnium also induces significant shifts and relative intensity changes in the FTIR and Raman spectra for some bands, which was ascribed to a higher acidity of hafnium compared to zirconium. After exposure to iodine, UiO-66(Hf) showed the best loading capacity (285 $g.mol^{-1}$, followed by UiO-66(51% Hf) with 250 $g.mol^{-1}$, and by UiO-66(Zr) with 230 $g.mol^{-1}$). The Raman spectra recorded at the end of iodine exposure process show new bands in the 100-210 cm^{-1} region attributed to various iodine species. Chemometric analysis using MCR-ALS algorithm allowed the extraction of three spectra corresponding to I_3^-, "perturbed" I_2 and "free" I_2 and the evolution of these species as a function of time was correlated to the kinetic of I_2 to I_3^- transformation. The faster conversion is observed for UiO-66(Hf) followed by UiO-66(51% Hf), and by UiO-66(Zr). Furthermore, FTIR and Raman spectra of the samples obtained after iodine exposure showed that the oxo and hydroxyl groups of the inorganic clusters are perturbed in UiO-66(Hf) but not in UiO-66(Zr). These results reveal that the metal content of UiO-66 has an influence on the evolution of trapped iodine in UiO-66. In this context, since EPR spectra revealed that there is no redox

phenomenon in the metal cations (Hf^{4+} and Zr^{4+}) during the I_2 to I_3^- transformation, the smaller band gap of UiO-66(Hf) could explain the lower electron-hole recombination rates. This feature may favor the I_3^- formation at the same time that the higher acidity of Hf^{4+} helps to stabilize the I_3^- species in the $BDC^{\bullet+}$ radical.

5. SUPPORTING INFORMATION

Structure of UiO-66 compounds, schematic of filtration bench using during iodine evolution tests, EDS spectra and elemental mapping, particle size distribution, Raman and FTIR bands evolution, adsorption kinetics plotted according to the LDF model, higher achieved Raman intensities after I_2 contact, Raman spectra displaying the CH stretching range.

6. ACKNOWLEDGMENTS

The “Fonds Européen de Développement Régional” (FEDER), the “Centre National de la Recherche Scientifique” (CNRS), the “Région Hauts de France”, and the “Ministère de l’Education Nationale de l’Enseignement Supérieur et de la Recherche” are acknowledged for the funding of X-ray diffractometers from the Chevreul Institute platform. The “Plateforme de Microscopie Électronique de Lille” (PMEL) is acknowledged for the support provided in SEM and EDS techniques. The authors acknowledge the Characterization platform for the FT Raman facilities and support. Dr. Aurélien Moncomble and Dr. Till Bousquet are acknowledged by their valuable contribution to the discussion of the mechanism model proposed in this work. V. Alaimo is recognized for ICP-OES analysis. P. H. M. A. would like to thank the University of Lille for the PhD grant.

7. REFERENCES

(1) Carlsson, J.; Forssell Aronsson, E.; Hietala, S.-O.; Stigbrand, T.; Tennvall, J. Tumour Therapy with Radionuclides: Assessment of Progress and Problems. *Radiother. Oncol.* **2003**, *66* (2), 107–117. https://doi.org/https://doi.org/10.1016/S0167-8140(02)00374-2.

(2) Narra, V. R.; Howell, R. W.; Harapanhalli, R. S.; Sastry, K. S.; Rao, D. V. Radiotoxicity of Some Iodine-123, Iodine-125 and Iodine-131-Labeled Compounds in Mouse Testes: Implications for Radiopharmaceutical Design. *J. Nucl. Med.* **1992**, *33* (12), 2196—2201.

(3) Riley, B. J.; Vienna, J. D.; Strachan, D. M.; McCloy, J. S.; Jerden, J. L. Materials and Processes for the Effective Capture and Immobilization of Radioiodine: A Review. *Journal of Nuclear Materials*. 2016, pp 307–326. https://doi.org/10.1016/j.jnucmat.2015.11.038.

(4) Pesce, L.; Kopp, P. Iodide Transport: Implications for Health and Disease. *Int. J. Pediatr. Endocrinol.* **2014**, *2014* (1), 1–12. https://doi.org/10.1186/1687-9856-2014-8.

(5) Takemura, T.; Nakamura, H.; Takigawa, M.; Kondo, H.; Satomura, T.; Miyasaka, T.; Nakajima, T. A Numerical Simulation of Global Transport of Atmospheric Particles Emitted from the Fukushima Daiichi Nuclear Power Plant. *Sci. Online Lett. Atmos.* **2011**, *7* (1), 101–104. https://doi.org/10.2151/sola.2011-026.

(6) Férey, G. Hybrid Porous Solids: Past, Present, Future. *Chem. Soc. Rev.* **2008**, *37* (1), 191–214. https://doi.org/10.1039/b618320b.

(7) Janiak, C.; Vieth, J. K. MOFs, MILs and More: Concepts, Properties and Applications for Porous Coordination Networks (PCNs). *New J. Chem.* **2010**, *34* (11), 2366–2388. https://doi.org/10.1039/c0nj00275e.

(8) Assaad, T.; Assfour, B. Metal Organic Framework MIL-101 for Radioiodine Capture and Storage. *J. Nucl. Mater.* **2017**, *493*, 6–11. https://doi.org/10.1016/j.jnucmat.2017.05.036.

(9) Chen, Q.; He, Q.; Lv, M.; Xu, Y.; Yang, H.; Liu, X.; Wei, F. Selective Adsorption of Cationic Dyes by UiO-66-NH 2. *Appl. Surf. Sci.* **2015**, *327*, 77–85. https://doi.org/10.1016/j.apsusc.2014.11.103.

(10) Kim, M.; Cahill, J. F.; Fei, H.; Prather, K. A.; Cohen, S. M. Postsynthetic Ligand and Cation Exchange in Robust Metal-Organic Frameworks. *J. Am. Chem. Soc.* **2012**, *134* (43),

18082–18088. https://doi.org/10.1021/ja3079219.

(11) Bai, Y.; Dou, Y.; Xie, L. H.; Rutledge, W.; Li, J. R.; Zhou, H. C. Zr-Based Metal-Organic Frameworks: Design, Synthesis, Structure, and Applications. *Chem. Soc. Rev.* **2016**, *45* (8), 2327–2367. https://doi.org/10.1039/c5cs00837a.

(12) Cavka, J. H.; Jakobsen, S.; Olsbye, U.; Guillou, N.; Lamberti, C.; Bordiga, S.; Lillerud, K. P. A New Zirconium Inorganic Building Brick Forming Metal Organic Frameworks with Exceptional Stability. *J. Am. Chem. Soc.* **2008**, *130* (42), 13850–13851. https://doi.org/10.1021/ja8057953.

(13) Valenzano, L.; Civalleri, B.; Chavan, S.; Bordiga, S.; Nilsen, M. H.; Jakobsen, S.; Lillerud, K. P.; Lamberti, C. Disclosing the Complex Structure of UiO-66 Metal Organic Framework: A Synergic Combination of Experiment and Theory. *Chem. Mater.* **2011**, *23* (7), 1700–1718. https://doi.org/10.1021/cm1022882.

(14) Jakobsen, S.; Gianolio, D.; Wragg, D. S.; Nilsen, M. H.; Emerich, H.; Bordiga, S.; Lamberti, C.; Olsbye, U.; Tilset, M.; Lillerud, K. P. Structural Determination of a Highly Stable Metal-Organic Framework with Possible Application to Interim Radioactive Waste Scavenging: Hf-UiO-66. *Phys. Rev. B - Condens. Matter Mater. Phys.* **2012**, *86* (12), 1–11. https://doi.org/10.1103/PhysRevB.86.125429.

(15) Rogge, S. M. J.; Yot, P. G.; Jacobsen, J.; Muniz-Miranda, F.; Vandenbrande, S.; Gosch, J.; Ortiz, V.; Collings, I. E.; Devautour-Vinot, S.; Maurin, G.; Stock, N.; Van Speybroeck, V. Charting the Metal-Dependent High-Pressure Stability of Bimetallic UiO-66 Materials. *ACS Mater. Lett.* **2020**, *2* (4), 438–445. https://doi.org/10.1021/acsmaterialslett.0c00042.

(16) Beyzavi, M. H.; Klet, R. C.; Tussupbayev, S.; Borycz, J.; Vermeulen, N. A.; Cramer, C. J.; Stoddart, J. F.; Hupp, J. T.; Farha, O. K. A Hafnium-Based Metal-Organic Framework as an Efficient and Multifunctional Catalyst for Facile CO2 Fixation and Regioselective and Enantioretentive Epoxide Activation. *J. Am. Chem. Soc.* **2014**, *136* (45), 15861–15864. https://doi.org/10.1021/ja508626n.

(17) Klet, R. C.; Liu, Y.; Wang, T. C.; Hupp, J. T.; Farha, O. K. Evaluation of Brønsted Acidity

and Proton Topology in Zr- and Hf-Based Metal-Organic Frameworks Using Potentiometric Acid-Base Titration. *J. Mater. Chem. A* **2016**, *4* (4), 1479–1485. https://doi.org/10.1039/c5ta07687k.

(18) Bakuru, V. R.; Churipard, S. R.; Maradur, S. P.; Kalidindi, S. B. Exploring the Brønsted Acidity of UiO-66 (Zr, Ce, Hf) Metal-Organic Frameworks for Efficient Solketal Synthesis from Glycerol Acetalization. *Dalt. Trans.* **2019**, *48* (3), 843–847. https://doi.org/10.1039/c8dt03512a.

(19) Leloire, M.; Dhainaut, J.; Devaux, P.; Leroy, O.; Desjonqueres, H.; Poirier, S.; Nerisson, P.; Cantrel, L.; Royer, S.; Loiseau, T.; Volkringer, C. Stability and Radioactive Gaseous Iodine-131 Retention Capacity of Binderless UiO-66-NH2 Granules under Severe Nuclear Accidental Conditions. *J. Hazard. Mater.* **2021**, *416*, 125890. https://doi.org/https://doi.org/10.1016/j.jhazmat.2021.125890.

(20) Leloire, M.; Walshe, C.; Devaux, P.; Giovine, R.; Duval, S.; Bousquet, T.; Chibani, S.; Paul, J.; Moissette, A.; Vezin, H.; Nerisson, P.; Cantrel, L.; Volkringer, C.; Loiseau, T. Capture of Gaseous Iodine in Isoreticular Zirconium- Based UiO- n Metal- Organic Frameworks: Influence of Amino Functionalization, DFT Calculations, Raman and EPR Spectroscopic Investigation. *Chem. – A Eur. J.* **2022**, *28* (14), e202104437. https://doi.org/10.1002/chem.202104437.

(21) Yasin, A. S.; Li, J.; Wu, N.; Musho, T. Study of the Inorganic Substitution in a Functionalized UiO-66 Metal-Organic Framework. *Phys. Chem. Chem. Phys.* **2016**, *18* (18), 12748–12754. https://doi.org/10.1039/c5cp08070c.

(22) Tauc, J. Optical Properties and Electronic Structure of Amorphous Ge and Si. *Mater. Res. Bull.* **1968**, *3* (1), 37–46. https://doi.org/https://doi.org/10.1016/0025-5408(68)90023-8.

(23) Kubelka, P.; Munk, F. An Article on Optics of Paint Layers. *Z. Tech. Phys.* **1931**, *12* (1930), 593–601.

(24) Yang, L. M.; Ganz, E.; Svelle, S.; Tilset, M. Computational Exploration of Newly Synthesized Zirconium Metal-Organic Frameworks UiO-66, -67, -68 and Analogues. *J.*

Mater. Chem. C **2014**, *2* (34), 7111–7125. https://doi.org/10.1039/c4tc00902a.

(25) Hendrickx, K.; Vanpoucke, D. E. P.; Leus, K.; Lejaeghere, K.; Van Yperen-De Deyne, A.; Van Speybroeck, V.; Van Der Voort, P.; Hemelsoet, K. Understanding Intrinsic Light Absorption Properties of UiO-66 Frameworks: A Combined Theoretical and Experimental Study. *Inorg. Chem.* **2015**, *54* (22), 10701–10710. https://doi.org/10.1021/acs.inorgchem.5b01593.

(26) Nethercot, A. H. Prediction of Fermi Energies and Photoelectric Thresholds Based on Electronegativity Concepts. *Phys. Rev. Lett.* **1974**, *33* (18), 1088–1091. https://doi.org/10.1103/PhysRevLett.33.1088.

(27) Mulliken, R. S. A New Electroaffinity Scale; Together with Data on Valence States and on Valence Ionization Potentials and Electron Affinities. *J. Chem. Phys.* **1934**, *2* (11), 782–793. https://doi.org/10.1063/1.1749394.

(28) Sircar, S.; Hufton, J. R. Why Does the Linear Driving Force Model for Adsorption Kinetics Work? *Adsorption* **2000**, *6* (2), 137–147. https://doi.org/10.1023/A:1008965317983.

(29) Leloire, M.; Walshe, C.; Devaux, P.; Giovine, R.; Duval, S.; Bousquet, T.; Chibani, S.; Paul, J.-F.; Moissette, A.; Vezin, H.; Nerisson, P.; Cantrel, L.; Volkringer, C.; Loiseau, T. Capture of Gaseous Iodine in Isoreticular Zirconium-Based UiO-n Metal-Organic Frameworks: Influence of Amino Functionalization, DFT Calculations, Raman and EPR Spectroscopic Investigation. *Chem. – A Eur. J.* **2022**, *28* (14), e202104437. https://doi.org/https://doi.org/10.1002/chem.202104437.

(30) Jaumot, J.; de Juan, A.; Tauler, R. MCR-ALS GUI 2.0: New Features and Applications. *Chemom. Intell. Lab. Syst.* **2015**, *140*, 1–12. https://doi.org/10.1016/j.chemolab.2014.10.003.

(31) Wu, R.; Qian, X.; Zhou, K.; Liu, H.; Yadian, B.; Wei, J.; Zhu, H.; Huang, Y. Highly Dispersed Au Nanoparticles Immobilized on Zr-Based Metal-Organic Frameworks as Heterostructured Catalyst for CO Oxidation. *J. Mater. Chem. A* **2013**, *1* (45), 14294–14299. https://doi.org/10.1039/C3TA13114A.

(32) Petříček, V.; Dušek, M.; Palatinus, L. Crystallographic Computing System JANA2006: General Features: *Zeitschrift für Krist. - Cryst. Mater.* **2014**, *229* (5), 345–352. https://doi.org/doi:10.1515/zkri-2014-1737.

(33) Shannon, R. D. Revised Effective Ionic Radii and Systematic Studies of Interatomic Distances in Halides and Chalcogenides. *Acta Crystallogr. Sect. A Cryst. physics, diffraction, Theor. Gen. Crystallogr.* **1976**, *32* (5), 751–767. https://doi.org/10.1107/S0567739476001551.

(34) Islamoglu, T.; Ray, D.; Li, P.; Majewski, M. B.; Akpinar, I.; Zhang, X.; Cramer, C. J.; Gagliardi, L.; Farha, O. K. From Transition Metals to Lanthanides to Actinides: Metal-Mediated Tuning of Electronic Properties of Isostructural Metal-Organic Frameworks. *Inorg. Chem.* **2018**, *57* (21), 13246–13251. https://doi.org/10.1021/acs.inorgchem.8b01748.

(35) Jeong, N. C.; Lee, J. S.; Tae, E. L.; Lee, Y. J.; Yoon, K. B. Acidity Scale for Metal Oxides and Sanderson's Electronegativities of Lanthanide Elements. *Angew. Chemie - Int. Ed.* **2008**, *47* (52), 10128–10132. https://doi.org/10.1002/anie.200803837.

(36) Nasalevich, M. A.; Hendon, C. H.; Santaclara, J. G.; Svane, K.; Van Der Linden, B.; Veber, S. L.; Fedin, M. V.; Houtepen, A. J.; Van Der Veen, M. A.; Kapteijn, F.; Walsh, A.; Gascon, J. Electronic Origins of Photocatalytic Activity in D0 Metal Organic Frameworks. *Sci. Rep.* **2016**, *6* (November 2015), 1–9. https://doi.org/10.1038/srep23676.

(37) Horiuchi, Y.; Nishida, H. Spectrophotometric Determination of Zirconium and Hafnium with 4-(2=Pyridylazo)Resorcino. *Bunseki Kagaku* **1967**, *16* (1), 20–27. https://doi.org/10.2116/bunsekikagaku.16.20.

(38) Chavan, S.; Vitillo, J. G.; Gianolio, D.; Zavorotynska, O.; Civalleri, B.; Jakobsen, S.; Nilsen, M. H.; Valenzano, L.; Lamberti, C.; Lillerud, K. P.; Bordiga, S. H2 Storage in Isostructural UiO-67 and UiO-66 MOFs. *Phys. Chem. Chem. Phys.* **2012**, *14* (5), 1614–1626. https://doi.org/10.1039/c1cp23434j.

(39) Sing, K. S. W. Reporting Physisorption Data for Gas/Solid Systems with Special Reference to the Determination of Surface Area and Porosity. *Pure Appl. Chem.* **1982**, *54* (11), 2201–

2218. https://doi.org/10.1351/pac198557040603.

(40) Hu, Z.; Nalaparaju, A.; Peng, Y.; Jiang, J.; Zhao, D. Modulated Hydrothermal Synthesis of UiO-66(Hf)-Type Metal-Organic Frameworks for Optimal Carbon Dioxide Separation. *Inorg. Chem.* **2016**, *55* (3), 1134–1141. https://doi.org/10.1021/acs.inorgchem.5b02312.

(41) Hadjiivanov, K. I.; Panayotov, D. A.; Mihaylov, M. Y.; Ivanova, E. Z.; Chakarova, K. K.; Andonova, S. M.; Drenchev, N. L. Power of Infrared and Raman Spectroscopies to Characterize Metal-Organic Frameworks and Investigate Their Interaction with Guest Molecules. *Chem. Rev.* **2021**, *121* (3), 1286–1424. https://doi.org/10.1021/acs.chemrev.0c00487.

(42) Guan, Y.; Li, Y.; Zhou, J.; Zhang, T.; Ding, J.; Xie, Z.; Wang, L. Defect Engineering of Nanoscale Hf-Based Metal–Organic Frameworks for Highly Efficient Iodine Capture. *Inorg. Chem.* **2021**. https://doi.org/10.1021/acs.inorgchem.1c01120.

(43) Gardner, J. M.; Abrahamsson, M.; Farnum, B. H.; Meyer, G. J. Visible Light Generation of Iodine Atoms and I-I Bonds: Sensitized I- Oxidation and I3 - Photodissociation. *J. Am. Chem. Soc.* **2009**, *131* (44), 16206–16214.

(44) Yang, L.; Saavedra, S. S.; Armstrong, N. R. Sol-Gel-Based, Planar Waveguide Sensor for Gaseous Iodine. *Anal. Chem.* **1996**, *68* (11), 1834–1841. https://doi.org/10.1021/ac960033q.

(45) Bhowmik, B.; Jendrasiak, G. L.; Rosenberg, B. Charge Transfer Complexes of Lipids with Iodine. *Nat. Publ. Gr.* **1967**, *216*, 615–616.

(46) Walker, L. A.; Pullen, S.; Donovan, B.; Sension, R. J. On the Structure of Iodine Charge-Transfer Complexes in Solution. *Chem. Phys. Lett.* **1995**, *242* (1–2), 177–183. https://doi.org/10.1016/0009-2614(95)00683-U.

(47) Benesi, H. A.; Hildebrand, J. H. A Spectrophotometric Investigation of the Interaction of Iodine with Aromatic Hydrocarbons. *J. Am. Chem. Soc* **1949**, *71* (8), 2703–2707. https://doi.org/10.1021/ja01176a030.

(48) Guo, W.; Wang, D.; Hu, J.; Tang, Z. K.; Du, S. Raman Spectroscopy of Iodine Molecules

Trapped in Zeolite Crystals. *Appl. Phys. Lett.* **2011**, *98* (4), 2011–2014. https://doi.org/10.1063/1.3549194.

(49) Anderson, A.; Sun, T. S. Raman Spectra of Molecular Crystals I. Chlorine, Bromine, and Iodine. *Chem. Phys. Lett.* **1970**, *6* (6), 611–616. https://doi.org/10.1016/0009-2614(70)85239-3.

(50) Klaboe, P. The Raman Spectra of Some Iodine, Bromine, and Iodine Monochloride Charge-Transfer Complexes in Solution. *J. Am. Chem. Soc.* **1967**, *89* (15), 3667–3676. https://doi.org/10.1021/ja00991a001.

(51) Deplano, P.; Devillanova, F. A.; Ferraro, J. R.; Isaia, F.; Lippolis, V.; Mercuri, M. L. On the Use of Raman Spectroscopy in the Characterization of Iodine in Charge-Transfer Complexes. *Appl. Spectrosc.* **1992**, *46* (11), 1625–1629.

(52) Zhang, W.; Mu, Y.; He, X.; Chen, P.; Zhao, S.; Huang, C.; Wang, Y.; Chen, J. Robust Porous Polymers Bearing Phosphine Oxide/Chalcogenide Ligands for Volatile Iodine Capture. *Chem. Eng. J.* **2020**, *379* (June 2019), 122365. https://doi.org/10.1016/j.cej.2019.122365.

(53) Blake, A. J.; Devillanova, F. A.; Gould, R. O.; Li, W. S.; Lippolis, V.; Parsons, S.; Radek, C.; Schröder, M. Template Self-Assembly of Polyiodide Networks. *Chem. Soc. Rev.* **1998**, *27* (3), 195–205. https://doi.org/10.1039/a827195z.

(54) Lobanov, S. S.; Daly, J. A.; Goncharov, A. F.; Chan, X.; Ghose, S. K.; Zhong, H.; Ehm, L.; Kim, T.; Parise, J. B. Iodine in Metal-Organic Frameworks at High Pressure. *J. Phys. Chem. A* **2018**, *122* (29), 6109–6117. https://doi.org/10.1021/acs.jpca.8b05443.

(55) Morterra, C.; Giamello, E.; Orio, L.; Volante, M. Formation and Reactivity of Zr3+ Centers at the Surface of Vacuum-Activated Monoclinic Zirconia. *J. Phys. Chem.* **1990**, *94* (7), 3111–3116. https://doi.org/10.1021/j100370a067.

(56) Occhiuzzi, M.; Cordischi, D.; Dragone, R. Intrinsic and Extrinsic Paramagnetic Centers in Zirconia. *J. Phys. Chem. B* **2002**, *106* (48), 12464–12469. https://doi.org/10.1021/jp0206830.

(57) Miyajima, N.; Akatsu, T.; Ikoma, T.; Ito, O.; Rand, B.; Tanabe, Y.; Yasuda, E. Role of Charge-Transfer Complex with Iodine in the Modification of Coal Tar Pitch. *Carbon N. Y.* **2000**, *38* (13), 1831–1838. https://doi.org/10.1016/S0008-6223(00)00022-1.

(58) Hoffmann, M. R.; Martin, S. T.; Choi, W.; Bahnemann, D. W. Environmental Applications of Semiconductor Photocatalysis. *Chem. Rev.* **1995**, *95* (1), 69–96. https://doi.org/10.1021/cr00033a004.

(59) Andrade, P. H. M.; Gomes, A. L. M.; Palhares, H. G.; Volkringer, C. Post-Synthetic Modification of Aluminum Trimesate and Copper Trimesate with TiO 2 Nanoparticles for Photocatalytic Applications. **2022**. https://doi.org/10.1007/s10853-021-06842-w.

(60) Fox, M. A.; Dulay, M. T. Heterogeneous Photocatalysis. *Chem. Rev.* **1993**, *93* (1), 341–357. https://doi.org/10.1021/cr00017a016.

(61) Mancuso, J. L.; Mroz, A. M.; Le, K. N.; Hendon, C. H. Electronic Structure Modeling of Metal-Organic Frameworks. *Chem. Rev.* **2020**, *120* (16), 8641–8715. https://doi.org/10.1021/acs.chemrev.0c00148.

(62) Kolobov, N.; Goesten, M. G.; Gascon, J. Metal–Organic Frameworks: Molecules or Semiconductors in Photocatalysis? *Angew. Chemie - Int. Ed.* **2021**, *60* (50), 26038–26052. https://doi.org/10.1002/anie.202106342.

(63) Santiago Portillo, A.; Baldoví, H. G.; García Fernandez, M. T.; Navalón, S.; Atienzar, P.; Ferrer, B.; Alvaro, M.; Garcia, H.; Li, Z. Ti as Mediator in the Photoinduced Electron Transfer of Mixed-Metal NH2-UiO-66(Zr/Ti): Transient Absorption Spectroscopy Study and Application in Photovoltaic Cell. *J. Phys. Chem. C* **2017**, *121* (12), 7015–7024. https://doi.org/10.1021/acs.jpcc.6b13068.

(64) Jayram, J.; Xulu, B. A.; Jeena, V. Iodine/DMSO Promoted Oxidation of Benzylic Csp3–H Bonds to Diketones – A Mechanistic Investigation. *Tetrahedron* **2019**, *75* (43), 130617. https://doi.org/https://doi.org/10.1016/j.tet.2019.130617.

(65) Deplano, P.; Ferraro, J. R.; Mercuri, M. L.; Trogu, E. F. Structural and Raman Spectroscopic Studies as Complementary Tools in Elucidating the Nature of the Bonding in

Polyiodides and in Donor-I2 Adducts. *Coord. Chem. Rev.* **1999**, *188* (1), 71–95. https://doi.org/10.1016/S0010-8545(98)00238-0.

FIGURE CAPTIONS

Figure 1: On the left side: SEM images obtained for (a) UiO-66(Zr), (b) UiO-66(25% Hf), (c) UiO-66(51% Hf), (d) UiO-66(75% Hf), and (e) UiO-66(Hf). On the right side: EDS/elemental mapping of UiO-66(51% Hf), Hf $M_{\alpha 1}$ signal is displayed in purple and Zr $L_{\alpha 1}$ in light blue.

Figure 2: (a) powder XRD pattern of UiO-66(Zr) (black), UiO-66(25% Hf) (red), UiO-66(51% Hf) (blue), UiO-66(75% Hf) (green), and UiO-66(Hf) (purple) after activation. The zoom in displays the first two diffraction peaks for each compound, with the (111) and (200) planes; copper radiation. (b) cubic lattice parameter *a* refined by Le Bail analysis as a function of the Hf/Zr atomic ratio.

Figure 3: (a) UV-vis spectra and (b) Tauc plot for UiO-66(Zr) (black), UiO-66(25% Hf) (red), UiO-66(51% Hf) (blue), UiO-66(75% Hf) (green), and UiO-66(Hf) (purple).

Figure 4: N_2 adsorption/desorption isotherms for UiO-66(Zr) (black), UiO-66(25% Hf) (red), UiO-66(51% Hf) (blue), UiO-66(75% Hf) (green), and UiO-66(Hf) (purple).

Figure 5: Raman spectra of UiO-66(Zr) (black), UiO-66(25% Hf) (red), UiO-66(51% Hf) (blue), UiO-66(75% Hf) (green), and UiO-66(Hf) (purple).

Figure 6: FTIR spectra of UiO-66(Zr) (black), UiO-66(25% Hf) (red), UiO-66(51% Hf) (blue), UiO-66(75% Hf) (green), and UiO-66(Hf) (purple).

Figure 7: Adsorption kinetics of gaseous iodine during 16 hours in UiO-66(Zr) (black), UiO-66(25% Hf) (red), UiO-66(51% Hf) (blue), UiO-66(75% Hf) (green), and UiO-66(Hf) (purple).

The I_2 adsorption within the cell where the powdered UiO-66 samples were placed was performed at room temperature. The UV-Vis spectra were also collected at room temperature.

Figure 8: UV-vis spectra from the pure UiO-66 (black), from the I_2@UiO-66 after 30 minutes of atmosphere exposure (red), and from the I_2@ UiO-66 after 72 hours of ambient air exposure (blue) for: (a) UiO-66(Zr), (b) UiO-66(51% Hf) and (c) UiO-66(Hf).

Figure 9: Raman spectra of (a) I_2@UiO-66(Zr), (b) I_2@UiO-66(51% Hf) and (c) I_2@UiO-66(Hf) recorded as a function of time from 30 minutes to 3 days after the UiO-66 exposure to the iodine stream. The first measurement was made after 30 minutes of leaving the iodine bench (red). The following were taken each hour for the first 24 hours, each two hours for the next 24 hours, and each four hours for the last 24 hours. The spectra of the pristine UiO-66 are displayed in black and highlighted by an arrow. The bands highlighted in red reduce in intensity with time, while the green ones increase in intensity.

Figure 10: MCR-ALS spectra for the iodine species extracted from the successive collection of I_2@UiO-66 Raman spectra: "free" I_2 (black), "perturbed" I_2 (red), and I_3^- (blue), after being exposed under ambient air up to 72 hours.

Figure 11: I_3^- (115 cm^{-1}) and I_2 (173 cm^{-1}) (a) peak concentration profiles and (b) their first order derivative for I_2@UiO-66(Zr) (black), I_2@UiO-66(51% Hf) (red), and I_2@UiO-66(Hf) (blue).

Figure 12: (a) from top to bottom: FTIR spectra of UiO-66(Zr), UiO-66(51% Hf), and UiO-66(Hf). (b) from top to bottom: Raman spectra of UiO-66(Zr), UiO-66(51% Hf), and UiO-66(Hf). In black: the spectra of the pristine; in red: the spectra of the I_2@UiO-66 after 30 minutes under ambient atmosphere exposure; in blue: the spectra of the I_2@UiO-66 after 72h under ambient atmosphere exposure.

Figure 13: EPR spectra under irradiation at t = 0 h (black), at t = 10 h (red), and after the end of the irradiation at t = 72 hours for (a) I_2@UiO-66(Zr) and (b) I_2@UiO-66(Hf).

Figure 14: Proposed model for the mechanism of I_2 to I_3^- transformation within UiO-66 framework.

TABLE CAPTIONS

Table 1: Physical chemical properties of the UiO-66 compounds displaying the Hf/Zr weight percentage and atomic ratio, the crystallite size, the lattice parameter (*a*), the band gap values, the CBM and VBM positions, the SSA_{BET}, the microporous volume, and the iodine uptake after 16 hours. The values in parenthesis are ascribed to the standard deviation. The microporous volume should be considered as the total pore volume of the samples.

Table 2: FTIR and Raman bands assignments according to calculated animations of vibrations obtained by Valenzano *et. al.* [13] for UiO-66(Zr). They are available at the CRYSTAL Web site: "https://www.crystal.unito.it/vibs/uio66_hydro/".

Table 3: Fitted kinetic constants data for the UiO-66 compounds using the Liner Driving Force model [28].

Table 4: Wavenumbers and their corresponding band assignments for the three distinct iodine species using Raman spectroscopy from UiO-66 samples.

FIGURE 1:

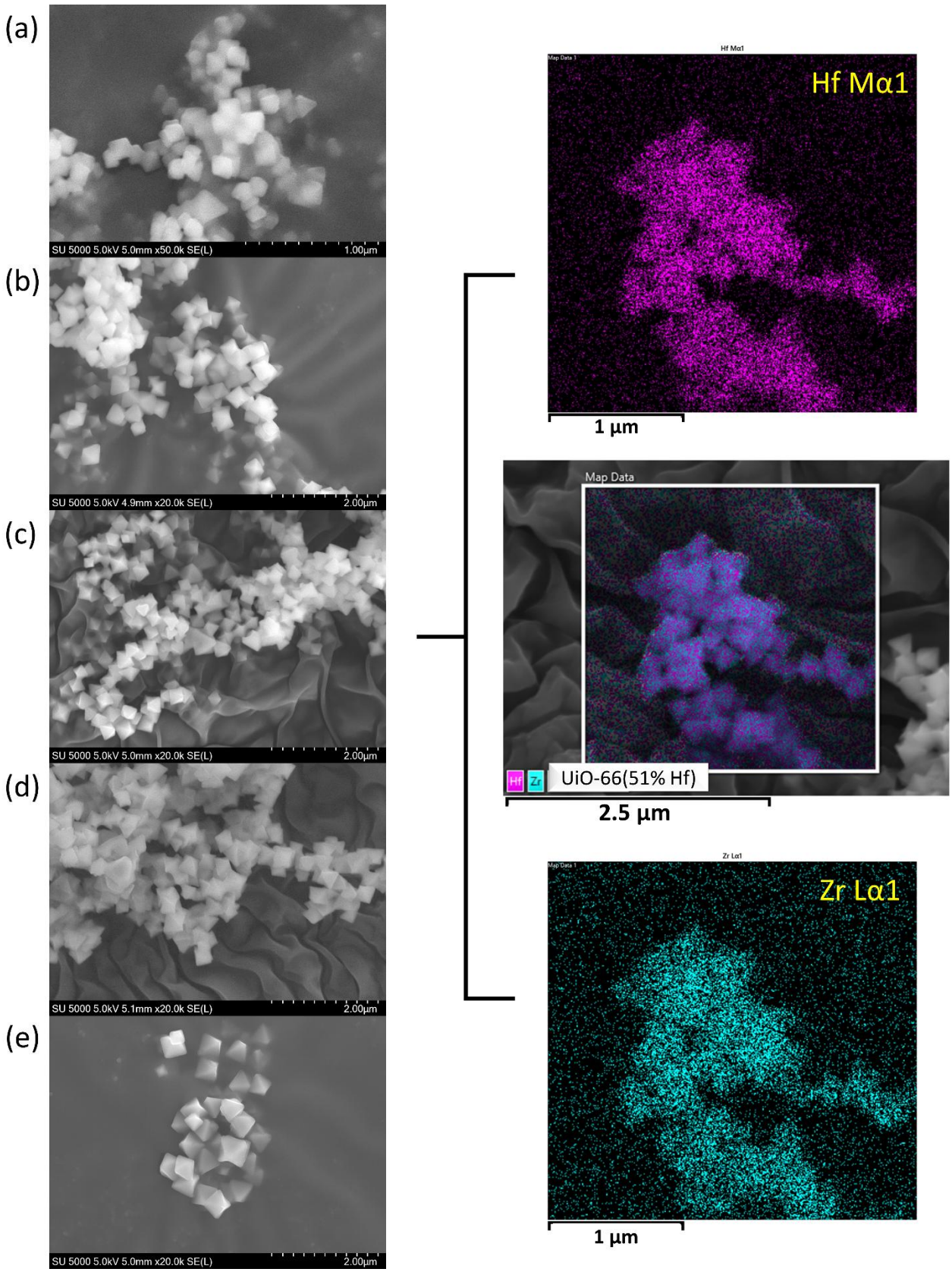
(a)
SU 5000 5.0kV 5.0mm x50.0k SE(L)
1.00µm
(b)
SU 5000 5.0kV 4.9mm x20.0k SE(L)
2.00µm
(c)
SU 5000 5.0kV 5.0mm x20.0k SE(L)
2.00µm
(d)
SU 5000 5.0kV 5.1mm x20.0k SE(L)
2.00µm
(e)
SU 5000 5.0kV 5.0mm x20.0k SE(L)
2.00µm
Hf Mα1
Hf Mα1
1 µm
Map Data
Hf
Zr
UiO-66(51% Hf)
2.5 µm
Zr Lα1
Zr Lα1
1 µm

FIGURE 2:

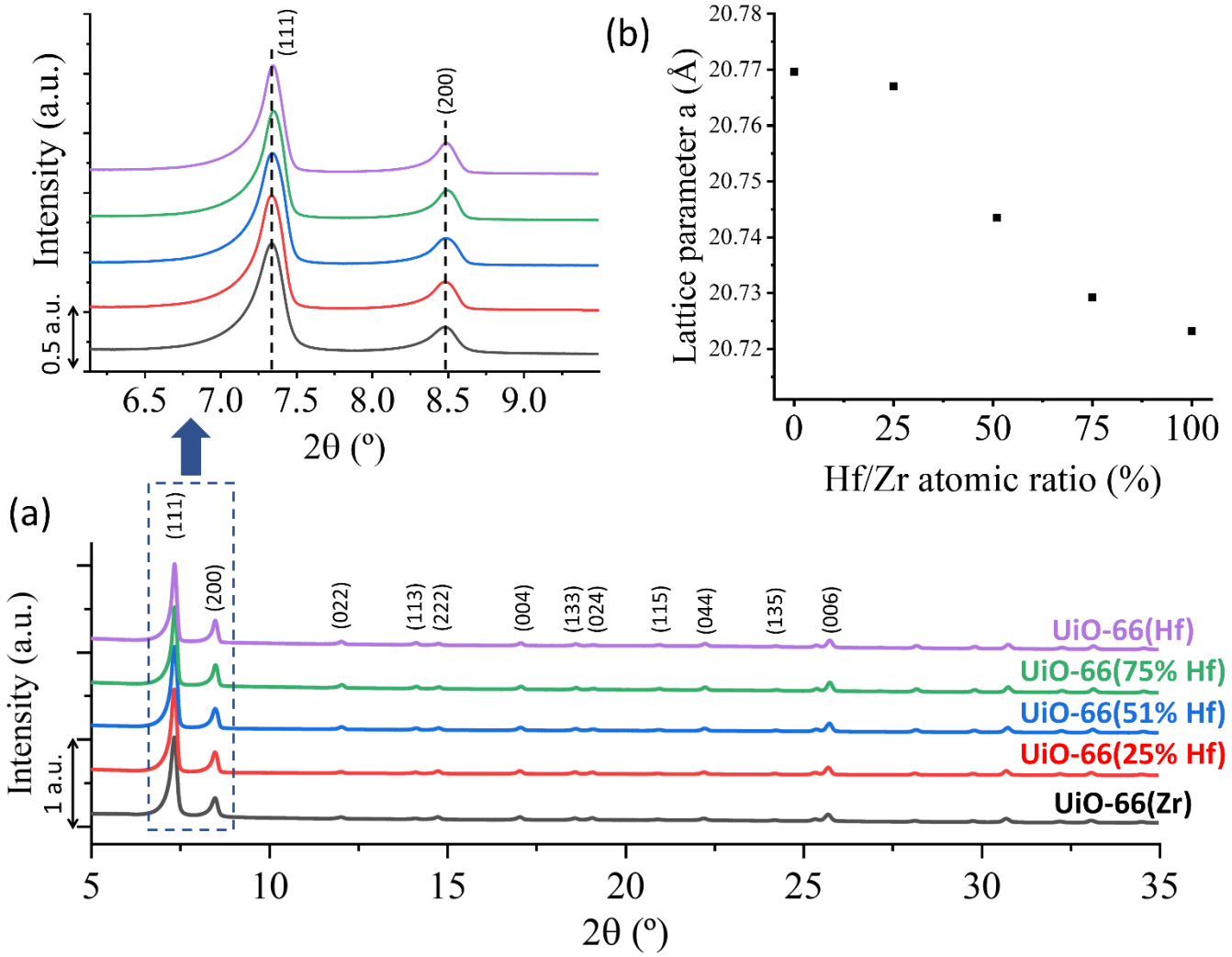
(a)
Intensity (a.u.)
1 a.u.
(111)
(200)
(022)
(113)
(222)
(004)
(133)
(024)
(115)
(044)
(135)
(006)
UiO-66(Hf)
UiO-66(75% Hf)
UiO-66(51% Hf)
UiO-66(25% Hf)
UiO-66(Zr)
2θ (°)
(b)
Lattice parameter a (Å)
Hf/Zr atomic ratio (%)

FIGURE 3:

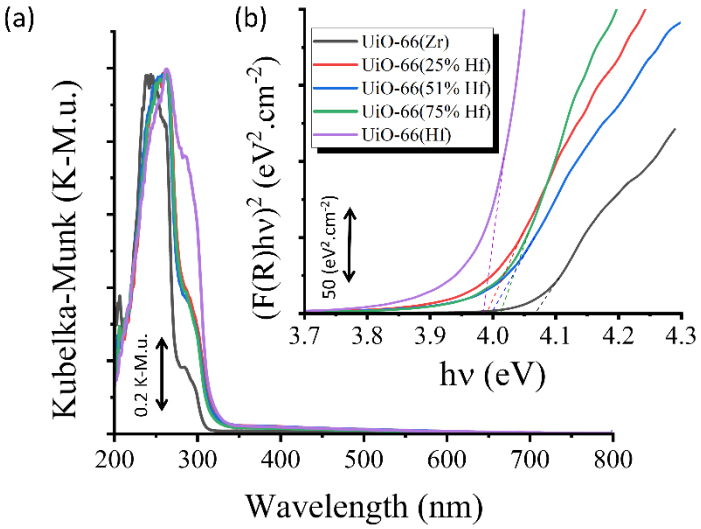

FIGURE 4:

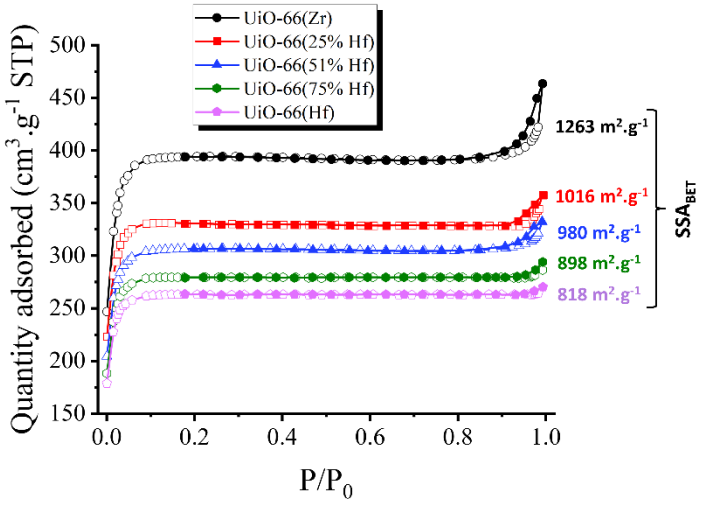

FIGURE 5:

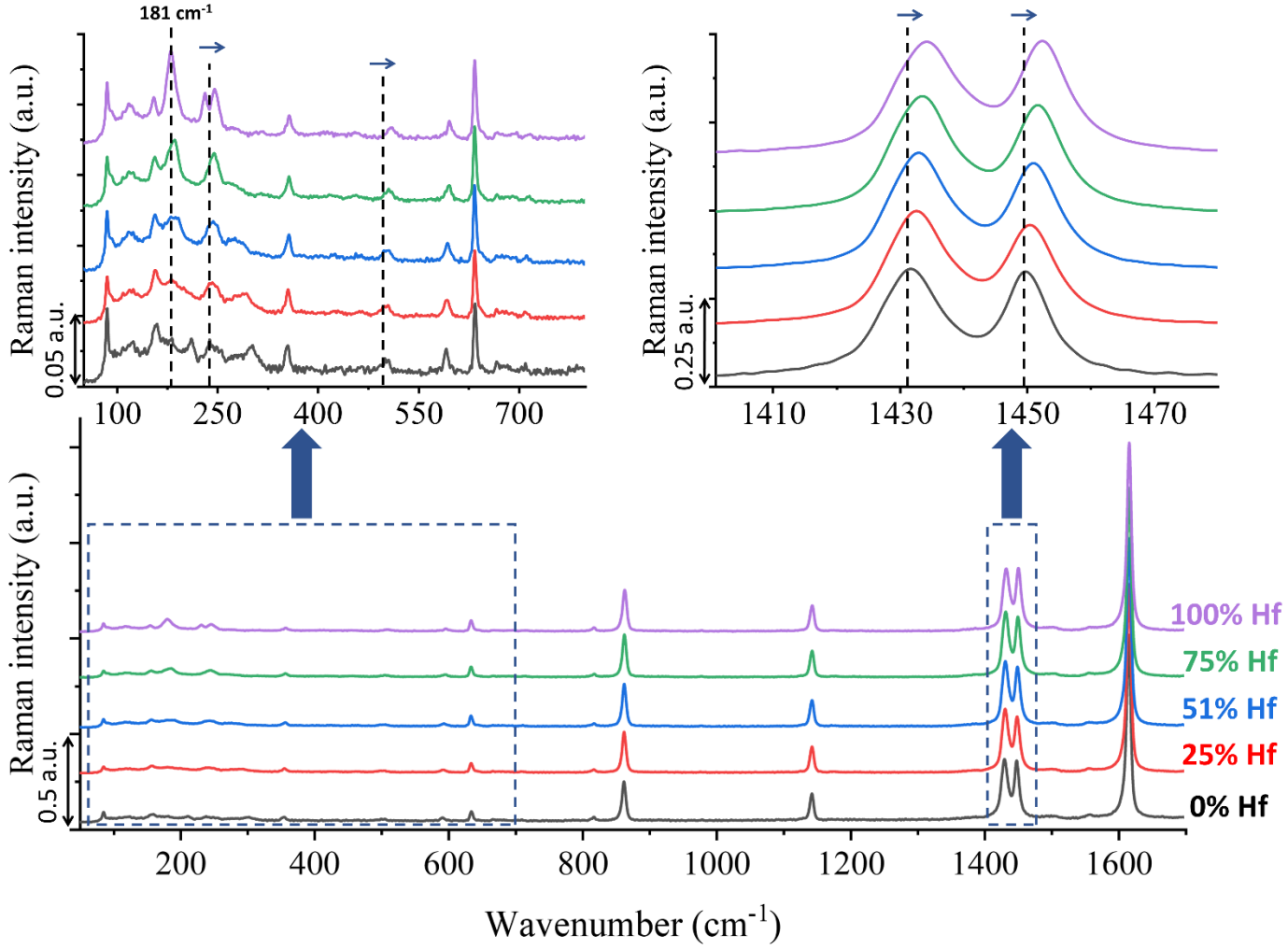
181 cm-1
Raman intensity (a.u.)
0.05 a.u.
100
250
400
550
700
Raman intensity (a.u.)
0.25 a.u.
1410
1430
1450
1470
Raman intensity (a.u.)
0.5 a.u.
100% Hf
75% Hf
51% Hf
25% Hf
0% Hf
200
400
600
800
1000
1200
1400
1600
Wavenumber (cm-1)

FIGURE 6

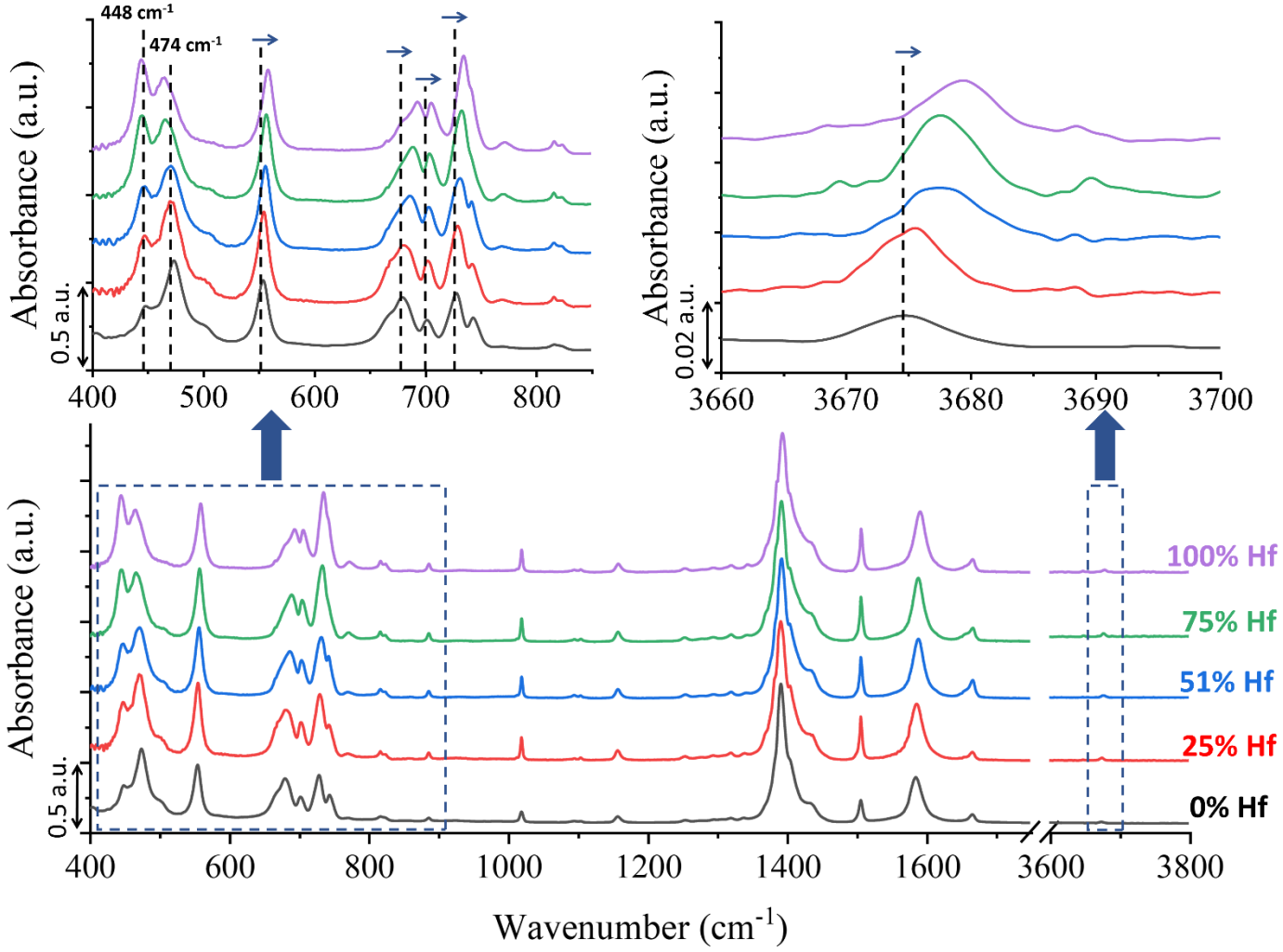

FIGURE 7:

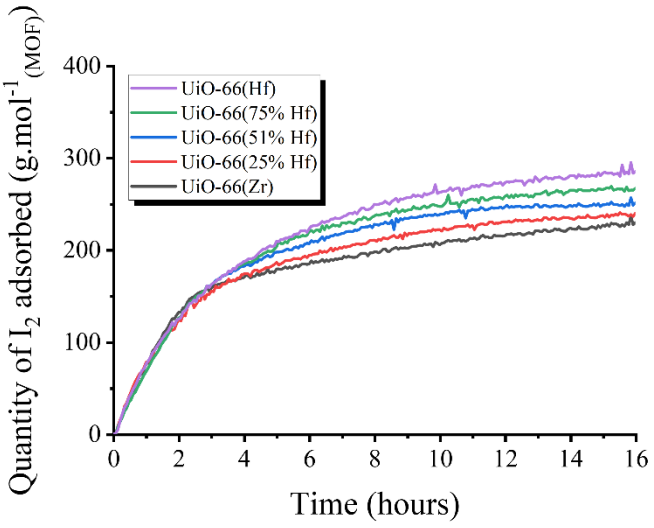

FIGURE 8:

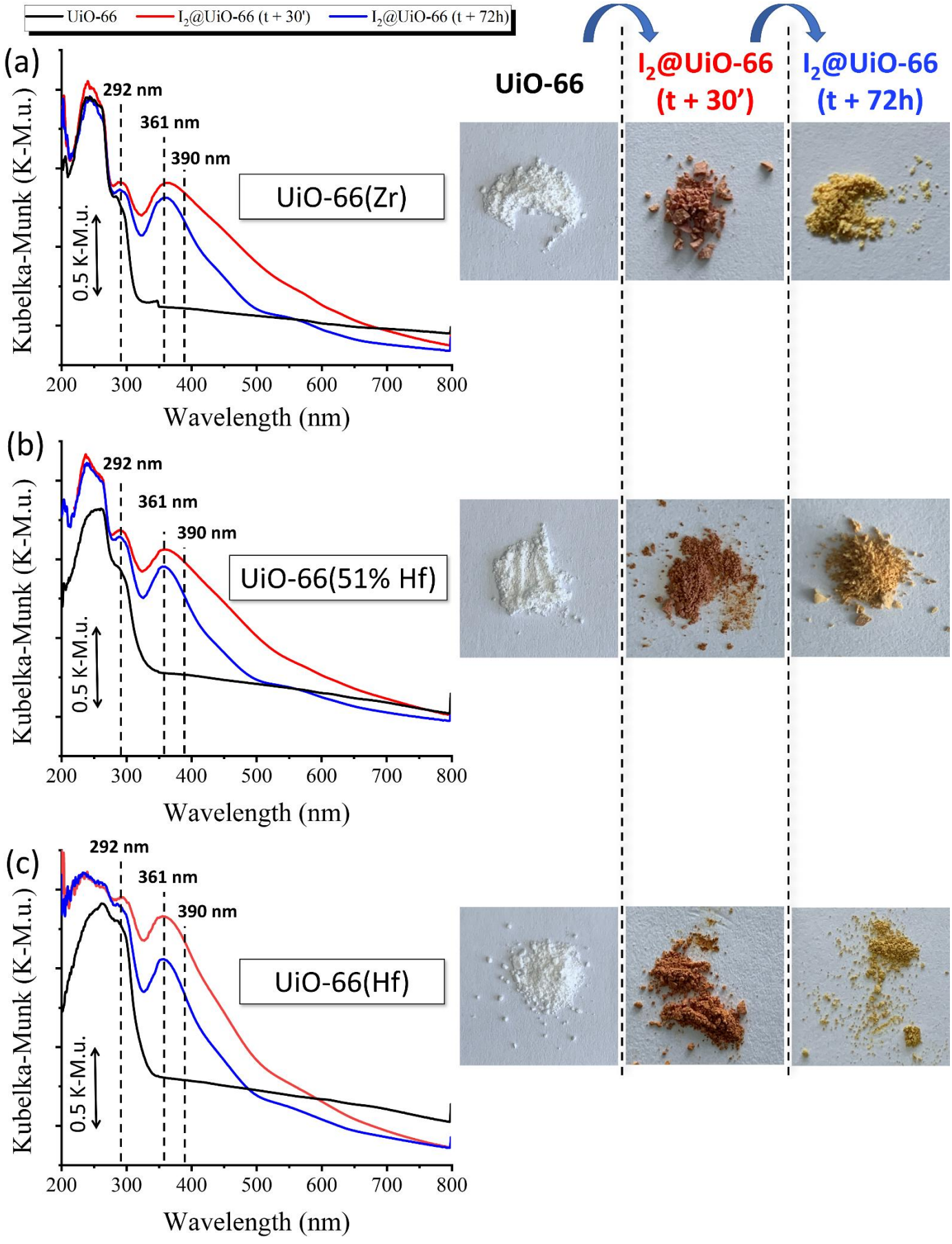
UiO-66
I2@UiO-66 (t + 30')
I2@UiO-66 (t + 72h)
(a)
292 nm
361 nm
390 nm
UiO-66(Zr)
0.5 K-M.u.
Kubelka-Munk (K-M.u.)
200 300 400 500 600 700 800
Wavelength (nm)
(b)
292 nm
361 nm
390 nm
UiO-66(51% Hf)
0.5 K-M.u.
Kubelka-Munk (K-M.u.)
200 300 400 500 600 700 800
Wavelength (nm)
(c)
292 nm
361 nm
390 nm
UiO-66(Hf)
0.5 K-M.u.
Kubelka-Munk (K-M.u.)
200 300 400 500 600 700 800
Wavelength (nm)
UiO-66
I2@UiO-66 (t + 30')
I2@UiO-66 (t + 72h)

FIGURE 9

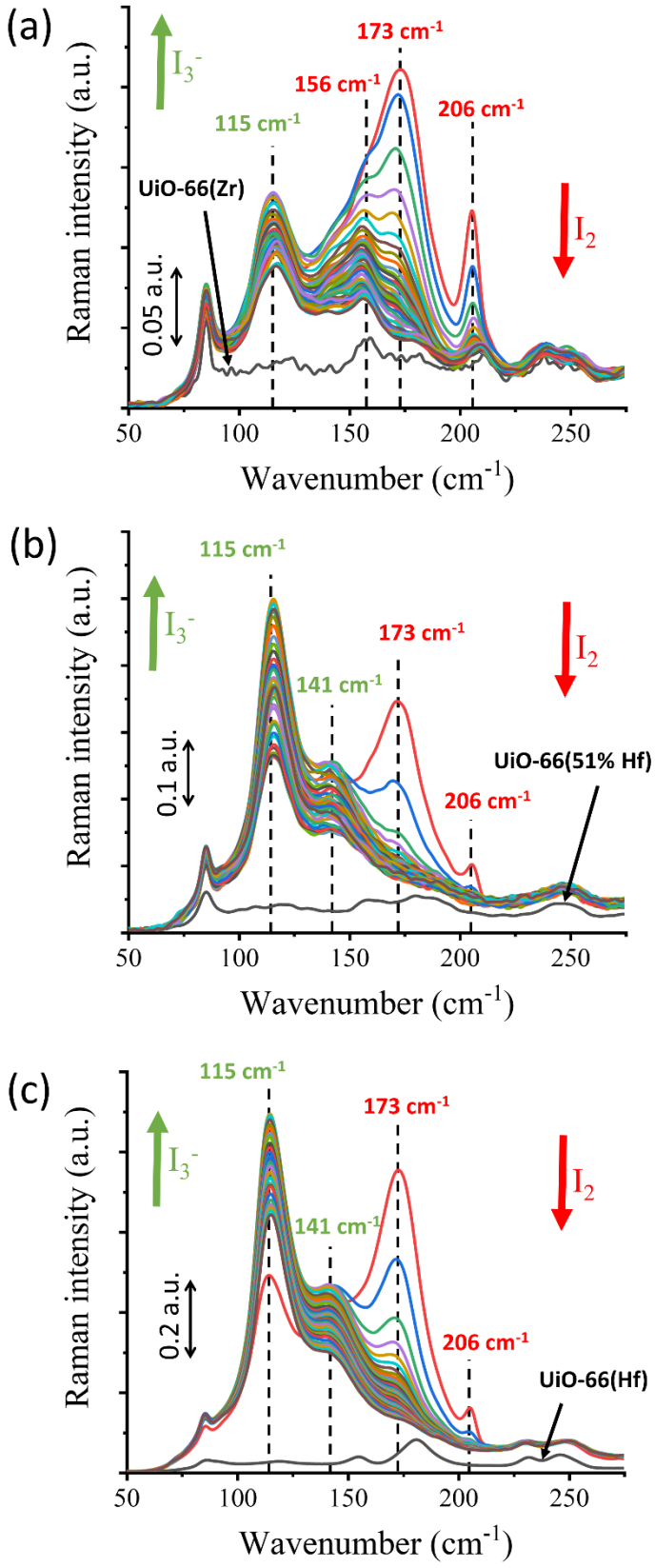
(a)
Raman intensity (a.u.)
I_3^-
173 cm^{-1}
156 cm^{-1}
206 cm^{-1}
115 cm^{-1}
UiO-66(Zr)
I_2
0.05 a.u.
50
100
150
200
250
Wavenumber (cm^{-1})
(b)
Raman intensity (a.u.)
115 cm^{-1}
I_3^-
173 cm^{-1}
I_2
141 cm^{-1}
UiO-66(51% Hf)
206 cm^{-1}
0.1 a.u.
50
100
150
200
250
Wavenumber (cm^{-1})
(c)
Raman intensity (a.u.)
115 cm^{-1}
173 cm^{-1}
I_3^-
I_2
141 cm^{-1}
206 cm^{-1}
UiO-66(Hf)
0.2 a.u.
50
100
150
200
250
Wavenumber (cm^{-1})

FIGURE 10

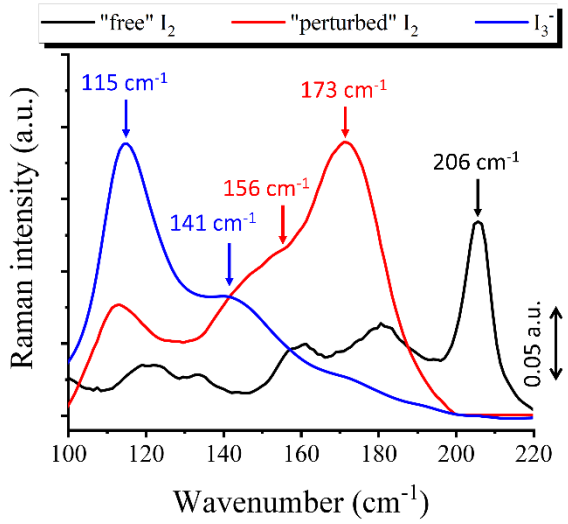

FIGURE 11:

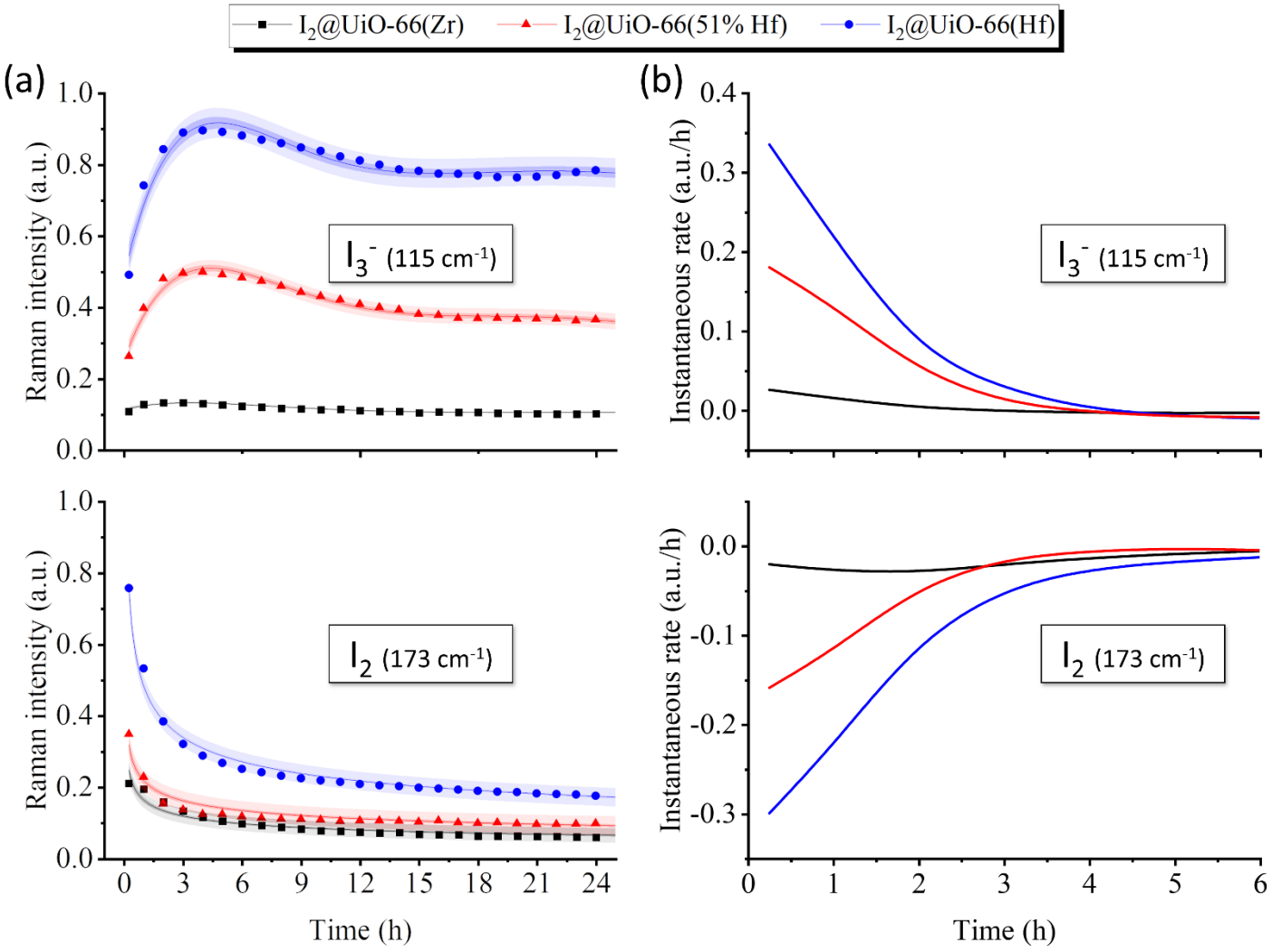

FIGURE 12:

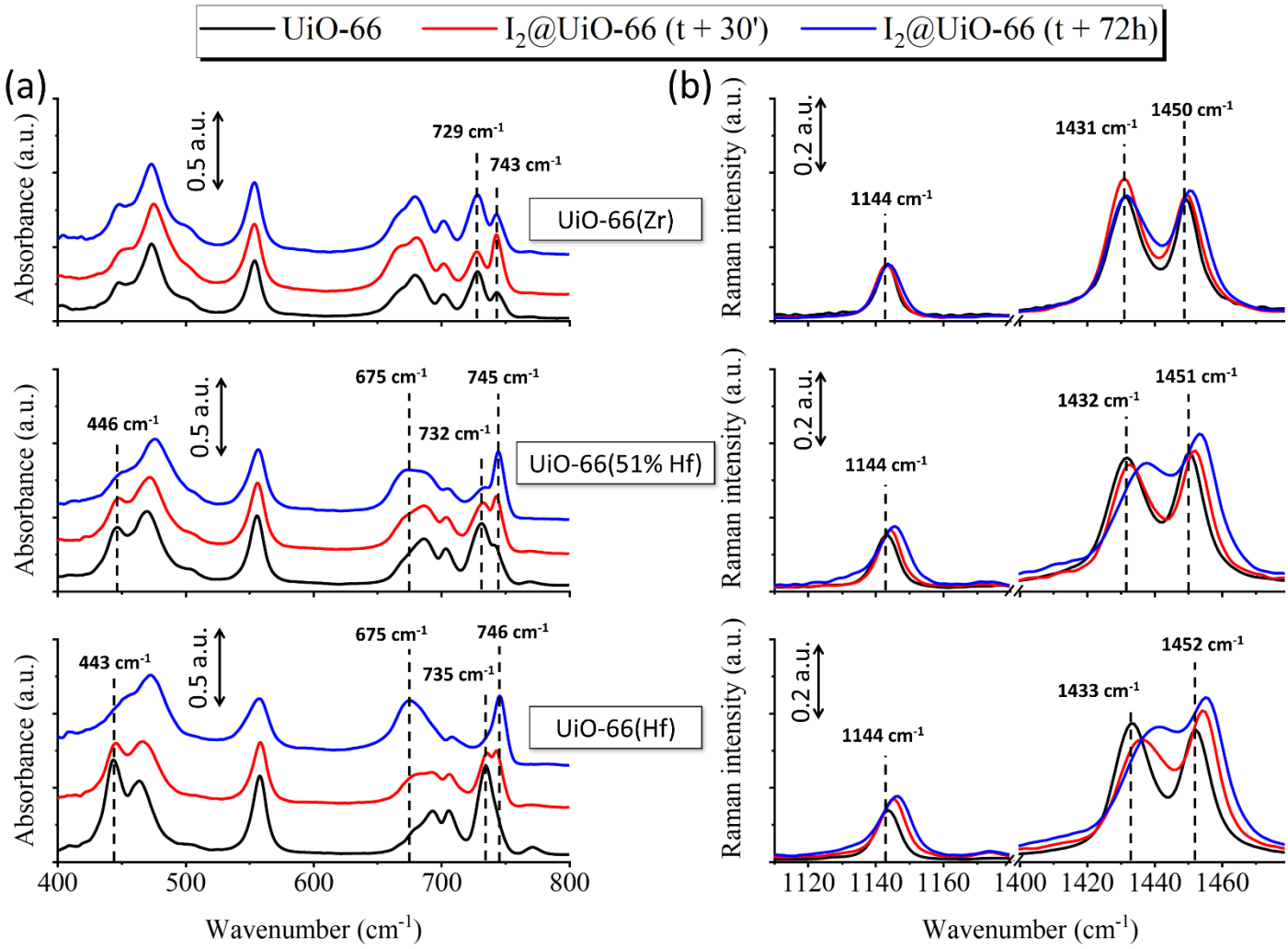
UiO-66
I2@UiO-66 (t + 30')
I2@UiO-66 (t + 72h)
(a)
(b)
Absorbance (a.u.)
Raman intensity (a.u.)
0.5 a.u.
0.2 a.u.
729 cm-1
743 cm-1
1144 cm-1
1431 cm-1
1450 cm-1
UiO-66(Zr)
446 cm-1
675 cm-1
745 cm-1
732 cm-1
1144 cm-1
1432 cm-1
1451 cm-1
UiO-66(51% Hf)
443 cm-1
675 cm-1
746 cm-1
735 cm-1
1144 cm-1
1433 cm-1
1452 cm-1
UiO-66(Hf)
400
500
600
700
800
1120
1140
1160
1400
1420
1440
1460
Wavenumber (cm-1)
Wavenumber (cm-1)

FIGURE 13:

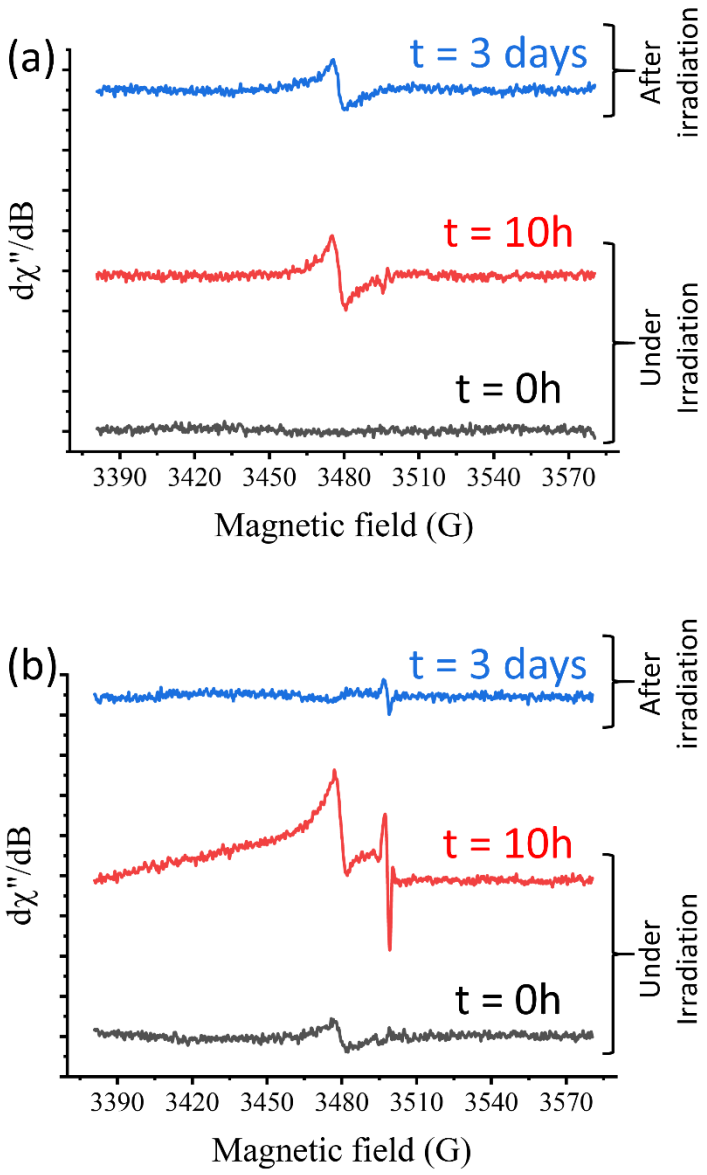
(a)
t = 3 days
After irradiation
t = 10h
t = 0h
Under Irradiation
dχ''/dB
3390 3420 3450 3480 3510 3540 3570
Magnetic field (G)
(b)
t = 3 days
After irradiation
t = 10h
t = 0h
Under Irradiation
dχ''/dB
3390 3420 3450 3480 3510 3540 3570
Magnetic field (G)

FIGURE 14:

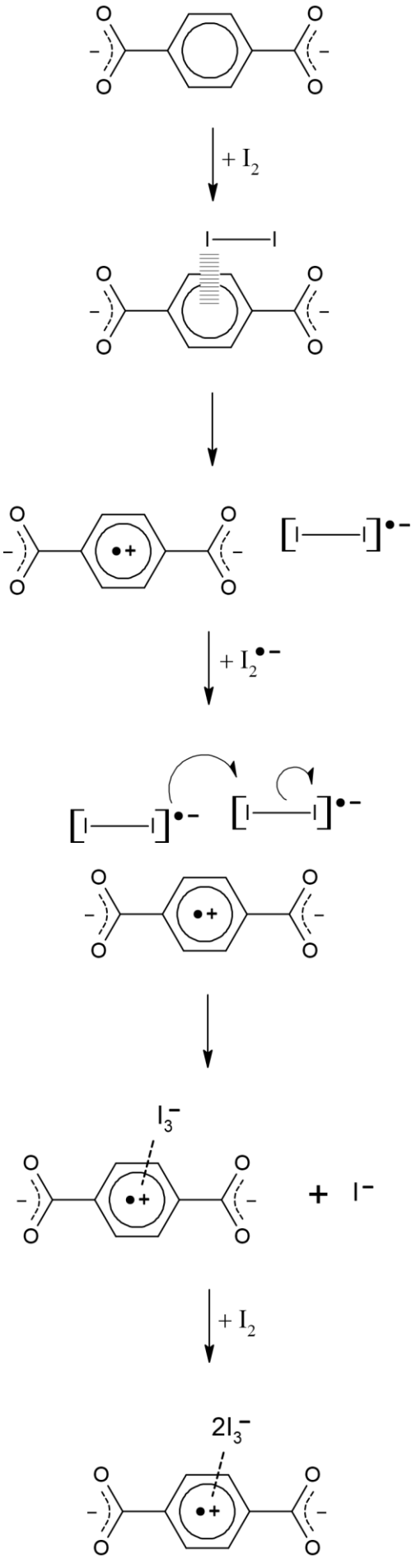

TABLE 1:

MOF	ICP-EOS ($\%_{wt}$)		Metal content ($\%_{at}$)				Crystallite size Φ	Lattice parameter *a*	E_g	E_{VB}	E_{CB}	$SSA_{(BET)}$		Microporous volume		Quantity of I_2 adsorbed after 16h	
			ICP-EOS		EDS												
	Hf	Zr	Hf	Zr	Hf	Zr	(nm)	(Å)	(eV)	(eV vs. SHE)		($m^2.g^{-1}$)	($km^2.mol^{-1}$)	($cm^3.g^{-1}$)	($cm^3.mol^{-1}$)	($mg.g^{-1}$)	($g.mol^{-1}$)
UiO-66(Zr)	0	32.3	0	100	0	100	100 – 250	20.7696(8)	4.07	4.15	0.08	1262(33)	2.1	0.598(28)	995	138	230
UiO-66 (Hf/Zr = 1:3)	14.7	22.2	25.0	75.0	19.4	80.6	110 – 530	20.7670(6)	3.99	4.11	0.12	1016(29)	1.8	0.530(26)	936	132	240
UiO-66 (Hf/Zr = 1:1)	28.9	14.4	51.0	49.0	41.0	59.0	130 – 1,110	20.7435(6)	4.00	4.12	0.12	980(25)	1.8	0.463(27)	870	126	250
UiO-66 (Hf/Zr = 3:1)	40.7	6.8	75.3	24.7	70.2	29.8	150 – 2,210	20.7292(4)	4.01	4.12	0.11	898(26)	1.8	0.460(28)	935	128	267
UiO-66(Hf)	53.3	0	100	0	100	0	180 – 3,330	20.7232(7)	3.98	4.11	0.13	818(24)	1.8	0.408(29)	893	130	285

TABLE 2:

Wavenumber (cm-1)					Bands assignment
Calculated [13]	FTIR (this work)		Raman (this work)		
UiO-66(Zr)	UiO-66(Zr)	UiO-66(Hf)	UiO-66(Zr)	UiO-66(Hf)	
73 (1)	–	–	85	85	Lattice torsion mode
127 (1), (2)	–	–	118	118	Linker rocking mode
163 (1)	–	–	156	156	Cluster torsion mode
196 (1)	–	–	181	181	Linker to metal-cluster in-plane bending + μ_3–O bending
206 (1), (2)	–	–	231	–	O–C–O translation mode
237 (1)	–	–	238	247	Linker to metal-cluster out of plane bending + M–(OH)–M bending
272 (1)	–	–	270	–	O–C–O torsion mode
358 (1)	–	–	355	355	Carboxylate to aromatic ring in-plane bending + carboxylate to metal-cluster rocking
447 (1), (2)	448	448	–	–	μ_3–OH antiphase stretching
470 (1), (2)	474	474	–	–	μ_3–OH in-phase stretching
501 (1)	–	–	500	509	μ_3–O and μ_3–OH in-phase bending (cluster breathing)
556 (1), (2)	554	558	–	–	M–(OC) asymmetric stretching
593 (1)	–	–	591	591	M–(OC) symmetric stretching
648 (1)	–	–	635	635	Aromatic ring in-plane bending
673 (1), (2)	679	693	667	667	μ_3–O stretching
711 (1), (2)	702	706	–	–	μ_3–OH bending + O–C–O bending + C=C–(COO) bending
718 (1), (2)	729	735	–	–	Aromatic ring torsion mode
771 (1), (2)	771	771	–	–	μ_3–OH bending + out of plane (C=C)–H bending (in-phase)
814 (1), (2)	816	816	816	816	μ_3–OH bending + out of plane (C=C)–H bending (antiphase)
875 (1)	–	–	862	862	C=C(COO) symmetric stretching (in-phase)
1023 (1)	1019	1019	–	–	Out of plane, antiphase (C=C)–H bending
1164 (1)	–	–	1143	1143	Aromatic ring breathing + in-plane symmetric (C=C)–H bending
1165 (1), (2)	1158	1158	–	–	In-plane symmetric (C=C)–H bending + C–O symmetric stretching
1367 (1), (2)	1392	1392	–	–	C=C(COO) asymmetric stretching
1408 (1), (2)	1405	1405	–	–	C–O symmetric stretching + C–C asymmetric stretching
1439 (1), (2)	1435	1435	1431	1434	In-plane asymmetric (C=C)–H bending + asymmetric C=C stretching
1474 (1)	–	–	1449	1452	C–C symmetric stretching
1539 (1), (2)	1507	1507	–	–	C=C symmetric stretching (antiphase) + in plane symmetric (C=C)–H bending
1607 (1), (2)	1591	1591	1618	1618	C–O asymmetric stretching
1665 (1), (2)	1666	1666	–	–	C=C symmetric stretching
3853 (1), (2)	3675	3680	–	–	OH stretching

(1) the vibration mode is active in Raman spectroscopy. (2) the vibration mode is active in FTIR spectroscopy.

TABLE 3:

UiO-66(M)	k_{LDF} (h^{-1})	R^2	t (*F(t)* = 0.90)[(a)]	t (*F(t)* = 0.99)[(a)]
Zr	0.323(5)	0.943	7 h 8 min	14 h 15 min
25% Hf	0.308(3)	0.981	7 h 29 min	14 h 57 min
51% Hf	0.318(2)	0.995	7 h 14 min	14 h 59 min
75% Hf	0.292(1)	0.997	7 h 53 min	15 h 46 min
Hf	0.267(1)	0.996	8 h 37 min	17 h 15 min

(a) t = time necessary to reach *F(t)* = 0.90 or *F(t)* = 0.99 from LDF fit

TABLE 4:

Wavenumber (cm^{-1})		Bands assignment	Reference
Literature	This work		
200-210	206	"free" I_2 inside the pores	[48]
150-180	156, 173	"perturbed" iodine	[51]
112, 143	115, 141	I_3^-	[65]